

# The connection between high-redshift galaxies and Lyman $\alpha$ transmission in the Sherwood-Relics simulations of patchy reionisation

Luke Conaboy<sup>1</sup> , James S. Bolton<sup>1</sup> , Laura C. Keating<sup>2</sup> , Martin G. Haehnelt<sup>3</sup> , Girish Kulkarni<sup>4</sup>   
and Ewald Puchwein<sup>5</sup> 

<sup>1</sup>*School of Physics and Astronomy, The University of Nottingham, University Park, Nottingham, NG7 2RD, UK*

<sup>2</sup>*Institute for Astronomy, University of Edinburgh, Blackford Hill, Edinburgh, EH9 3HJ, UK*

<sup>3</sup>*Kavli Institute for Cosmology and Institute of Astronomy, Madingley Road, Cambridge, CB3 0HA, UK*

<sup>4</sup>*Tata Institute of Fundamental Research, Homi Bhabha Road, Mumbai 400005, India*

<sup>5</sup>*Leibniz-Institut für Astrophysik Potsdam, An der Sternwarte 16, 14482 Potsdam, Germany*

Accepted XXX. Received YYY; in original form ZZZ

## ABSTRACT

Recent work has suggested that, during reionisation, spatial variations in the ionising radiation field should produce enhanced Ly  $\alpha$  forest transmission at distances of tens of comoving Mpc from high-redshift galaxies. We demonstrate that the Sherwood-Relics suite of hybrid radiation-hydrodynamical simulations are qualitatively consistent with this interpretation. The shape of the galaxy–Ly  $\alpha$  transmission cross-correlation is sensitive to both the mass of the haloes hosting the galaxies and the volume averaged fraction of neutral hydrogen in the IGM,  $\bar{x}_{\text{HI}}$ . The reported excess Ly  $\alpha$  forest transmission on scales  $r \sim 10$  cMpc at  $\langle z \rangle \approx 5.2$  – as measured using C IV absorbers as proxies for high-redshift galaxies – is quantitatively reproduced by Sherwood-Relics at  $z = 6$  if we assume the galaxies that produce ionising photons are hosted in haloes with mass  $M_{\text{h}} \geq 10^{10} h^{-1} M_{\odot}$ . However, this redshift mismatch is equivalent to requiring  $\bar{x}_{\text{HI}} \sim 0.1$  at  $z \approx 5.2$ , which is inconsistent with the observed Ly  $\alpha$  forest effective optical depth distribution. We speculate this tension may be partly resolved if the minimum C IV absorber host halo mass at  $z > 5$  is larger than  $M_{\text{h}} = 10^{10} h^{-1} M_{\odot}$ . After reionisation completes, relic IGM temperature fluctuations will continue to influence the shape of the cross-correlation on scales of a few comoving Mpc at  $4 \leq z \leq 5$ . Constraining the redshift evolution of the cross-correlation over this period may therefore provide further insight into the timing of reionisation.

**Key words:** methods: numerical – intergalactic medium – galaxies: high-redshift – quasars: absorption lines – large scale structure of Universe – dark ages, reionization, first stars

## 1 INTRODUCTION

Between the first hundred million years and the first billion years, the hydrogen gas permeating the Universe transitioned from cold and neutral to warm and (re)ionised. A wide variety of observational constraints place the midpoint of reionisation between  $7 \lesssim z \lesssim 8$  (e.g., Davies et al. 2018; Bañados et al. 2018; Greig et al. 2019; Jung et al. 2020; Planck Collaboration et al. 2020; Gaikwad et al. 2023; Jin et al. 2023; Āurovčíková et al. 2024; Umeda et al. 2024). The rapid evolution of the mean free path of Lyman-limit photons between  $5 < z < 6$  (Becker et al. 2021; Zhu et al. 2023; Satyavolu et al. 2024), the distribution of the Ly  $\alpha$  forest transmission (Bosman et al. 2022), and the presence of damping wings in the spectra of  $z < 6$  quasars (Becker et al. 2024; Spina et al. 2024; Zhu et al. 2024a) are furthermore consistent with the last neutral hydrogen islands persisting to  $z < 6$ . This suggests reionisation may have finished around  $z \approx 5.3$  (Kulkarni et al. 2019; Keating et al. 2020b,a; Nasir & D’Aloisio 2020).

Concurrently, *JWST* is opening up a new window on galaxy for-

mation at  $z \gtrsim 8$  (e.g., Naidu et al. 2022; Arrabal Haro et al. 2023; Castellano et al. 2024; Harikane et al. 2024; Zavala et al. 2024). Constraints from deep observations with *JWST* suggest that faint, low-mass galaxies are efficient at producing ionising photons, and can provide the majority of the ionising photons required for reionisation (Atek et al. 2024; Saxena et al. 2024; Simmonds et al. 2024; Begley et al. 2024, although see also Gazagnes et al. 2024). The discovery of many faint AGN (e.g. Harikane et al. 2023) also means that a contribution to the ionising photon budget by faint AGN is plausible (Maiolino et al. 2024; Grazian et al. 2024; Madau et al. 2024; Asthana et al. 2024a).

A promising route for connecting the properties of the IGM with these high redshift ionising sources is a cross-correlation with intergalactic Ly  $\alpha$  transmission. At low redshifts ( $z < 5$ ), well after the end of reionisation, the galaxy–Ly  $\alpha$  transmission correlation has been extensively studied (Adelberger et al. 2005; Tummuangpak et al. 2014; Turner et al. 2014; Bielby et al. 2017; Matthee et al. 2024; Banerjee et al. 2024). The low-redshift ( $2 \lesssim z \lesssim 4$ ) picture that has emerged is one of a strong decrease in Ly  $\alpha$  transmission approaching galaxies, driven by enhanced overdensities and the clustering and infall of neutral hydrogen in the regions where these galaxies reside.

\* E-mail: luke.conaboy@nottingham.ac.uk

Models of this low-redshift deficit in transmission at small impact parameters ( $b \lesssim 1$  cMpc) also suggest that stellar feedback plays an important role in setting the level of Ly  $\alpha$  transmission (Meiksin et al. 2017; Sorini et al. 2020).

At higher redshifts, the picture is less clear. Kakiichi et al. (2018) used a small sample of spectroscopically-confirmed Lyman break galaxies (LBGs) at  $5.3 < z < 6.4$  in the field of a  $z = 6.42$  QSO to examine the impact of local ionisation on Ly  $\alpha$  transmission. They cross-correlated the positions of these LBGs with the Ly  $\alpha$  forest, finding that there was some evidence (tempered by the small sample size) for an enhancement of Ly  $\alpha$  transmission in proximity to galaxies. This enhancement they attributed not solely to the observed LBGs, but also to the ionising radiation produced by nearby, faint, and therefore undetected, sources. Meyer et al. (2019) computed the ID correlation between C IV absorbers and Ly  $\alpha$  transmission in the spectra of 25 QSOs at  $4.5 < z < 6.3$ , finding reduced transmission at  $r \lesssim 5 h^{-1}$  Mpc (qualitatively similar to the low-redshift results discussed previously, though quantitatively the deficit in transmission in Meyer et al. 2019 is somewhat stronger) and statistically-significant enhanced Ly  $\alpha$  transmission relative to the mean at distances of  $r \sim 10\text{--}30 h^{-1}$  Mpc. In a follow-up work, Meyer et al. (2020) characterised the galaxy–Ly  $\alpha$  transmission correlation at  $z \sim 6$ , but were unable to reproduce the findings of Meyer et al. (2019), which they attribute to a small sample size and noise. Finally, Kashino et al. (2023) reported a measurement of the galaxy–Ly  $\alpha$  transmission correlation from a single QSO sightline from the EIGER survey at  $5.3 < z < 5.7$  and  $5.7 < z < 6.14$ .

Modelling of the high-redshift galaxy–Ly  $\alpha$  transmission correlation using reionisation simulations has also returned a variety of results. Garaldi et al. (2019) performed the first examination of the transmission correlation in the high-redshift context, using the CROC simulations of cosmic reionisation (Gnedin 2014). Garaldi et al. (2019) compared the results of the CROC simulation to the Meyer et al. (2019) observational constraints, finding that their models show a reduction in transmission close to galaxies (in a similar fashion to the low- $z$  observations) but do not reproduce the enhanced transmission at larger radii reported by Meyer et al. (2019). Zhu et al. (2024b) performed a further analysis of the CROC simulations and confirmed the absence of an excess in transmission. In contrast, Garaldi et al. (2022) showed that, in the THESAN simulations (Kannan et al. 2022; Smith et al. 2022), the galaxy–Ly  $\alpha$  transmission correlation shows both reduced transmission close to galaxies and excess transmission at larger distances. This is qualitatively similar to Meyer et al. (2019), although good agreement with the Meyer et al. (2019) results occurs at a different (higher) redshift in the models. Garaldi et al. (2022) also demonstrated that, in the context of the THESAN model, the galaxy–Ly  $\alpha$  transmission correlation is largely independent of the source model when reionisation history is accounted for (e.g., by comparing the correlation at fixed neutral fraction  $x_{\text{HI}}$ , as opposed to fixed redshift). Recently, Garaldi & Bellscheidt (2024a) performed a deeper analysis of the galaxy–Ly  $\alpha$  transmission correlation in THESAN, focusing on its observability. They noted that the selection criteria for galaxies (e.g., C IV absorption, [O III] flux) appears to have little impact on the correlation in their models.

In this context, we examine the galaxy–Ly  $\alpha$  transmission correlation in the Sherwood-Relics<sup>1</sup> simulation suite (Puchwein et al. 2023). In this work we focus on the high-redshift ( $z \geq 4.2$ ) galaxy–Ly  $\alpha$  transmission correlation, at distances  $r \gtrsim$  few cMpc from galaxies. Sherwood-Relics has demonstrated excellent agreement with obser-

vations for a range of IGM properties at  $z \lesssim 6$  (see e.g., Gaikwad et al. 2020; Molaro et al. 2022; Feron et al. 2024). The simulations differ from other numerical models in several ways. First, they have been designed specifically for modelling the properties of the Ly  $\alpha$  forest at the tail end of reionisation, making them ideal for investigating the galaxy–Ly  $\alpha$  transmission correlation at  $z \sim 6$ . Second, instead of full radiation-hydrodynamics, Sherwood-Relics uses a novel hybrid radiative transfer (RT) scheme (see Sec. 2.1) that captures the hydrodynamical response of the gas to the inhomogeneous photoheating and photoionisation associated with reionisation. This allows different reionisation histories to be examined at relatively low computational cost.

The paper is structured as follows. In Sec. 2.1 we briefly describe the simulations used in this work, and in Sec. 2.2 we perform an initial examination of the Ly  $\alpha$  transmission around galaxies in our fiducial model to gain intuition. Next, in Sec. 3 we explore the galaxy–Ly  $\alpha$  transmission correlation in Sherwood-Relics, and in Sec. 4 we explore the effect of different modelling assumptions in an attempt to elucidate the physical origin of the galaxy–Ly  $\alpha$  transmission correlation, both during and after reionisation. Finally, we conclude in Sec. 5. We assume a flat  $\Lambda$ CDM cosmology with  $\Omega_{\Lambda} = 0.692$ ,  $\Omega_{\text{m}} = 0.318$ ,  $\Omega_{\text{b}} = 0.0482$ ,  $\sigma_8 = 0.829$ ,  $n_{\text{s}} = 0.961$  and  $h = 0.678$  (Planck Collaboration et al. 2014). Unless otherwise specified, distance units are comoving (and may be explicitly specified as such by the prefix ‘c’).

## 2 MODELLING Ly $\alpha$ TRANSMISSION

### 2.1 Sherwood-Relics simulations

The simulations used in this work form part of the Sherwood-Relics project (see Puchwein et al. 2023, for details). The Sherwood-Relics suite of simulations are a series of high-resolution cosmological hydrodynamical simulations performed using a modified version of P-GADGET-3 (itself a modified version of GADGET-2, described in Springel 2005). In this study, we use runs with box sizes of  $40 h^{-1}$  Mpc (40-2048) and  $160 h^{-1}$  Mpc (160-2048), each containing  $2 \times 2048^3$  particles. In addition, for testing the convergence of our results with mass resolution, we also employ variants of the  $40 h^{-1}$  Mpc box that are identical to 40-2048, except they were run with  $2 \times 1024^3$  (40-1024) and  $2 \times 512^3$  particles (40-512). See Table 1 for a summary of the runs used in this work.

The Sherwood-Relics project uses a novel hybrid radiative transfer (RT) scheme to capture the hydrodynamical effects of inhomogeneous reionisation, without incurring the expense of fully-coupled radiation-hydrodynamical (RHD) simulations. Here we briefly outline key points of the method, but for the full exposition see Puchwein et al. (2023). In this scheme, the monochromatic radiative transfer of UV photons is followed using the moment-based, M1-closure RT code ATON (Aubert & Teysseier 2008). ATON is run in post-processing mode (i.e. on a periodically refreshed, rather than continuously evolving, density field, meaning that the evolution of the density is not coupled to that of the radiation) on a base P-GADGET-3 simulation, with input snapshots spaced every  $\Delta t = 40$  Myr. From this ATON simulation, we extract three-dimensional maps of the inhomogeneous H I photoionisation rate  $\Gamma_{\text{HI}}$  at each redshift. These  $\Gamma_{\text{HI}}$  maps then serve as inputs to a new P-GADGET-3 simulation, thus allowing the hydrodynamic response of the gas to the spatially-varying radiation field to be captured, without running expensive RHD simulations. The luminosity of an ionising source is assumed to be proportional to its halo mass, and the minimum mass of ionising

<sup>1</sup> <https://www.nottingham.ac.uk/astronomy/sherwood-relics/>

**Table 1.** Overview of the Sherwood-Relics runs employed in this study (see also Puchwein et al. 2023). Listed in columns are: the name used to refer to the run; linear comoving box size in  $h^{-1}$  cMpc ( $L_{\text{box}}$ ); total initial number of dark matter and gas particles ( $N_{\text{part}}$ ); dark matter particle mass in  $h^{-1} M_{\odot}$  ( $M_{\text{d}}$ ); gas particle mass in  $h^{-1} M_{\odot}$  ( $M_{\text{g}}$ ); redshift at which the global volume-averaged neutral fraction drops below  $10^{-3}$  ( $z_{\text{r}}$ ), and the output redshifts for snapshots  $z_{\text{snap}}$ . The lowest redshift snapshot for all models is  $z = 4.2$ .

Name	$L_{\text{box}}$ ( $h^{-1}$ cMpc)	$N_{\text{part}}$	$M_{\text{d}}$ ( $h^{-1} M_{\odot}$ )	$M_{\text{g}}$ ( $h^{-1} M_{\odot}$ )	$z_{\text{r}}$	$z_{\text{mid}}$	$z_{\text{snap}}$
40-2048 (fiducial)	40	$2 \times 2048^3$	$5.37 \times 10^5$	$9.97 \times 10^4$	5.7	7.5	every $\Delta z = 0.2$
40-2048 (late)	40	$2 \times 2048^3$	$5.37 \times 10^5$	$9.97 \times 10^4$	5.3	7.2	$z = 7, 6, 5.4, 4.8, 4.2$
40-2048 (mid)	40	$2 \times 2048^3$	$5.37 \times 10^5$	$9.97 \times 10^4$	6.0	7.3	$z = 7, 6, 5.4, 4.8, 4.2$
40-2048 (early)	40	$2 \times 2048^3$	$5.37 \times 10^5$	$9.97 \times 10^4$	6.6	8.0	$z = 7, 6, 5.4, 4.8, 4.2$
40-1024	40	$2 \times 1024^3$	$4.30 \times 10^6$	$7.97 \times 10^5$	5.7	7.5	every $\Delta z = 0.2$
40-512	40	$2 \times 512^3$	$3.44 \times 10^7$	$6.38 \times 10^6$	5.7	7.5	every $\Delta z = 0.2$
160-2048	160	$2 \times 2048^3$	$3.44 \times 10^7$	$6.38 \times 10^6$	5.3	7.2	$z = 7, 6, 5.4, 4.8, 4.2$

sources is  $M_{\text{h}} > 10^9 h^{-1} M_{\odot}$ . Ionising photons have mean energy 18.6 eV, which corresponds to a blackbody spectrum with temperature  $T = 4 \times 10^4$  K. The exact emissivity of each halo is not a prediction but is determined by fixing the redshift evolution of the total ionising emissivity, thus allowing the exact reionisation history to be calibrated (Kulkarni et al. 2019; Keating et al. 2020b).

In Fig. 1 we show the redshift evolution of the volume-averaged neutral fraction  $\bar{x}_{\text{HI}}$  and the mean transmission,  $\bar{F}$ , of the Ly  $\alpha$  forest in  $50 h^{-1}$  cMpc skewers for all the models used in this work. Note that the 40-1024 and 40-512 models use the same reionisation history as the fiducial 40-2048 model. Two of the models we use are calibrated to match measurements of  $\bar{F}$ : the fiducial 40-2048 model is calibrated to the Bosman et al. (2018) and Eilers et al. (2018) measurements, while the 160-2048 model is calibrated to match the Bosman et al. (2022) measurements. In addition to the calibrated reionisation histories, we also use three other models where reionisation ends at:  $z_{\text{r}} = 5.3$  (late),  $z_{\text{r}} = 6.0$  (mid), and  $z_{\text{r}} = 6.7$  (early). These models are not calibrated to measurements of  $\bar{F}$ , but are useful for observing the effect of an altered reionisation history. Note also that despite using the same reionisation history as the fiducial 40-2048 model, differences in mass resolution mean that the 40-1024 and 40-512 models do not exactly match the Bosman et al. (2018) and Eilers et al. (2018) results.

The Sherwood-Relics project is primarily concerned with modelling the high-redshift IGM, and so does not include detailed sub-grid physics models for galaxy formation. Instead, a computationally-efficient density removal scheme – the ‘quick Ly  $\alpha$ ’ approach – is employed, where gas particles with overdensity  $\rho_{\text{g}}/\bar{\rho}_{\text{g}} = \Delta > 1000$  and temperature  $T < 10^5$  K are converted to collisionless star particles (Viel et al. 2004). The simulations do not include any prescription for stellar feedback. Halo finding is performed using the inbuilt friends-of-friends (FoF) halo finder with a linking length of 0.2 times the mean interparticle spacing (Springel 2005). When we discuss ‘halo masses’, we are referring to the total FoF group mass  $M_{\text{h}} = M_{\text{h,d}} + M_{\text{h,g}} + M_{\text{h},\star}$ , where  $M_{\text{h,d}}$ ,  $M_{\text{h,g}}$  and  $M_{\text{h},\star}$  are the dark matter, gas and stellar components of the FoF group, respectively.

Sightlines are drawn through the simulation volume to extract the relevant quantities for computing mock Ly  $\alpha$  absorption spectra. We draw 5000 such sightlines, with a spatial resolution of 28.8 ckpc (115.2 ckpc) for the  $40 h^{-1}$  Mpc ( $160 h^{-1}$  Mpc) box. These sightlines are then post-processed to compute the Ly  $\alpha$  optical depths, using the approximation to the Voigt line profile due to Tepper-García (2006) and including, unless otherwise stated, the effects of peculiar velocities.

## 2.2 Real-space Ly $\alpha$ transmission

Before proceeding further, to develop some intuition about the nature of the galaxy–Ly  $\alpha$  transmission correlation, following Kulkarni et al. (2015) we consider the real-space Ly  $\alpha$  transmission. We will return to examining the full line-of-sight calculation of Ly  $\alpha$  optical depths, including redshift space distortions, in Sec. 3. The real-space Ly  $\alpha$  transmission is defined as

$$F_{\text{real}} = \exp \left[ -\frac{3\lambda_{\alpha}^3 \Lambda_{\alpha}}{8\pi H(z)} x_{\text{HI}} \Delta \bar{n}_{\text{H}} \right], \quad (1)$$

where  $\lambda_{\alpha} = 1216 \text{ \AA}$  is the rest-frame Ly  $\alpha$  wavelength,  $\Lambda_{\alpha} = 6.265 \times 10^{-8} \text{ s}^{-1}$ ,  $H(z)$  is the Hubble parameter,  $\bar{n}_{\text{H}}$  is the mean number density of hydrogen,  $\Delta$  is the overdensity and  $x_{\text{HI}}$  is the neutral hydrogen fraction, which depends on both the photoionisation rate,  $\Gamma_{\text{HI}}$ , and the gas temperature,  $T$ . Note that Eq. (1) is equal to  $\exp(-\tau_{\text{GP}})$ , where  $\tau_{\text{GP}}$  is the Gunn–Peterson optical depth (Gunn & Peterson 1965) and, unlike the calculations performed in the rest of this work, Eq. (1) ignores the effect of peculiar velocities and thermal line broadening on the Ly  $\alpha$  optical depth, and assumes that the line profile is a Dirac delta function at  $\lambda = \lambda_{\alpha}$ .

We calculate  $F_{\text{real}}$  by first depositing the particles in the simulation onto a uniform grid; the Ly  $\alpha$  transmission can then be computed for each pixel independently. Next, we must select the haloes that host galaxies in the simulation. Measurements of the galaxy–Ly  $\alpha$  transmission correlation often use different methods for the detection of galaxies, such as C iv absorption or [O III] emission. Given these differing detection methods, it is not immediately clear how to relate the sources of absorption in the observations to the structures in our simulations. Meyer et al. (2019) used abundance matching arguments to relate the incidence of C iv absorbers per absorption distance  $dN/dX$  to the halo mass function and thus obtain an approximate lower mass limit on the haloes hosting these absorbers, finding  $M_{\text{h}} \gtrsim 10^{9.8} h^{-1} M_{\odot}$ . Their measurement of the C iv absorber bias is very uncertain, however, and is consistent with host halo masses as large as  $M_{\text{h}} \sim 10^{12.4} h^{-1} M_{\odot}$ . Pizzati et al. (2024) use the FLAMINGO simulations (Schaye et al. 2023) to reproduce observations of the cross-correlation of high- $z$  galaxies (selected through [O III] emission), finding that the characteristic host halo mass of an [O III] emitter is  $\approx 10^{10.7} h^{-1} M_{\odot}$ . However, Garaldi et al. (2022) and Garaldi & Bellscheidt (2024a) found that the exact choice of selection criteria (e.g. C iv column density or halo mass) makes only a small impact on the galaxy–Ly  $\alpha$  transmission correlation. Motivated by these arguments, here and throughout the rest of this work we therefore compute the galaxy–Ly  $\alpha$  transmission correlation for haloes with  $M_{\text{h}} \geq 10^{10} h^{-1} M_{\odot}$ , unless otherwise specified. Finally, we extract a slice of depth 115.2 ckpc for each

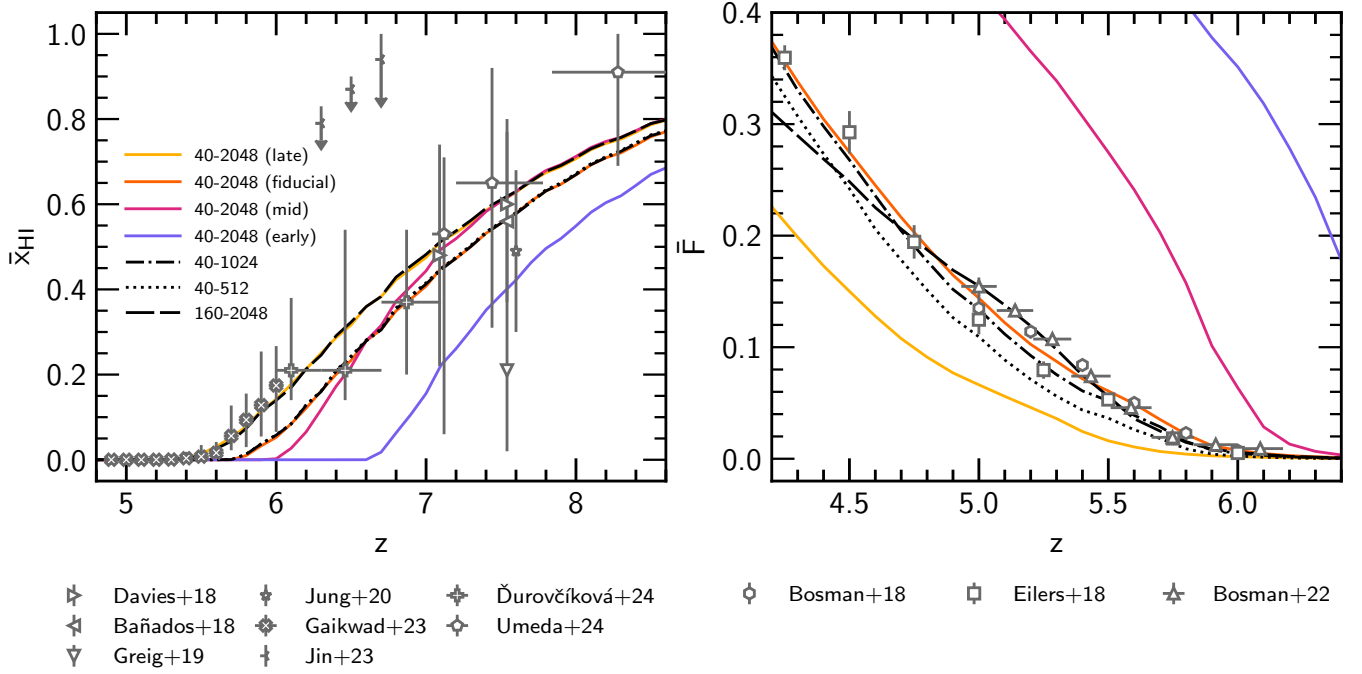


**Figure 1.** Left: evolution of the volume-averaged neutral fraction  $\bar{x}_{\text{HI}}$  in the 40-2048 (coloured solid), 40-1024 (dot-dashed), 40-512 (dotted) and 160-2048 (long-dashed) runs. For the 40-2048 run we show four different reionisation models: late (gold), fiducial (orange), mid (dark pink) and early (purple) – see Table 1 for details. Also shown are observational constraints on  $\bar{x}_{\text{HI}}$  derived from: the effective optical depth of the Ly  $\alpha$  forest (Gaikwad et al. 2023); quasar damping wings (Bañados et al. 2018; Davies et al. 2018; Greig et al. 2019; Āurovčíková et al. 2024, shown for the ATON model constraints); the Ly  $\alpha$  emitter equivalent width distribution (Jung et al. 2020); Ly  $\alpha$  and Ly  $\beta$  dark pixel fractions (Jin et al. 2023); and galaxy damping wings (Umeda et al. 2024). Right: the mean transmission in the Ly  $\alpha$  forest over  $50 h^{-1} \text{cMpc}$  skewers, with constraints from Bosman et al. (2018); Eilers et al. (2018); Bosman et al. (2022). The fiducial 40-2048 model is calibrated to reproduce the Bosman et al. (2018) and Eilers et al. (2018) results, while the 160-2048 model is calibrated to reproduce the Bosman et al. (2022) results.

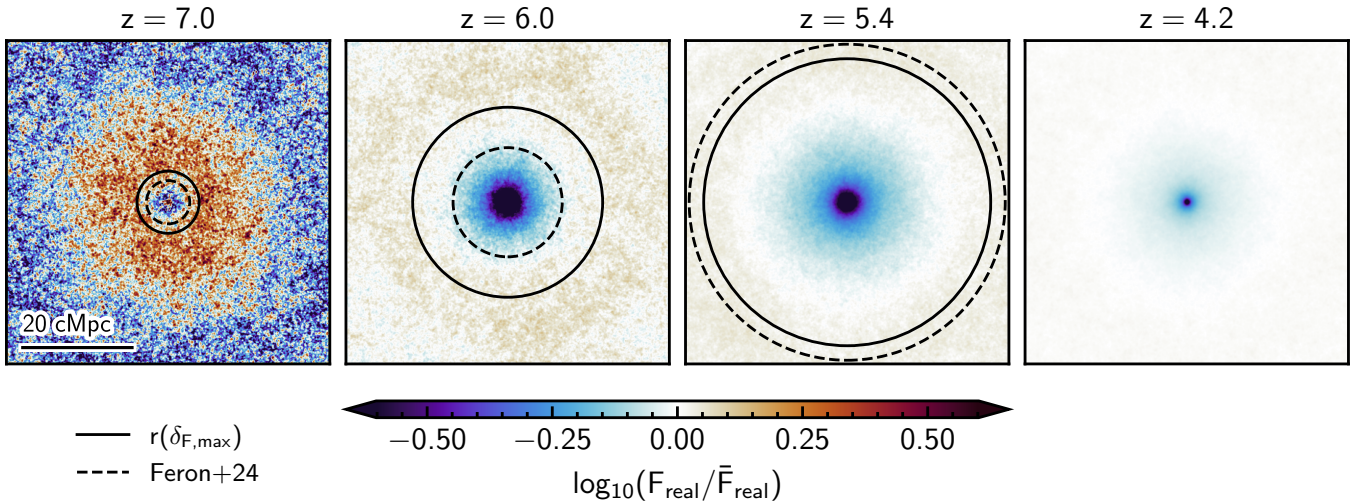


**Figure 2.** Logarithm of the normalised real-space Ly  $\alpha$  transmission in stacked slices, each centred on a halo with mass  $M_{\text{h}} \geq 10^{10} h^{-1} M_{\odot}$  for the fiducial 40-2048 model. Each slice has width  $40 h^{-1} \text{cMpc}$  and depth  $115.2 \text{ckpc}$ . We show the stacked transmission fluctuation at fixed redshifts of (from left to right)  $z = 7.0$ ,  $6.0$ ,  $5.4$  and  $4.2$ , where each stack is produced from 2,431, 4,540, 6,191 and 10,706 slices, respectively. To highlight the structure of the transmission correlation, we clip the dynamic range of the colour scale to be from  $\bar{F}_{\text{real}}/4$  to  $4\bar{F}_{\text{real}}$ , as indicated by the arrows on the colour bar. Also shown for comparison (see Sec. 3.3 for a discussion) is the distance at which the halo-Ly  $\alpha$  transmission correlation (calculated without including peculiar velocities) is largest ( $r(\delta F_{\text{max}})$ , black solid circle), and the mean free path of Lyman limit photons around haloes from Feron et al. (2024) ( $\Lambda_{\text{mfp}}$ , black dashed circle).



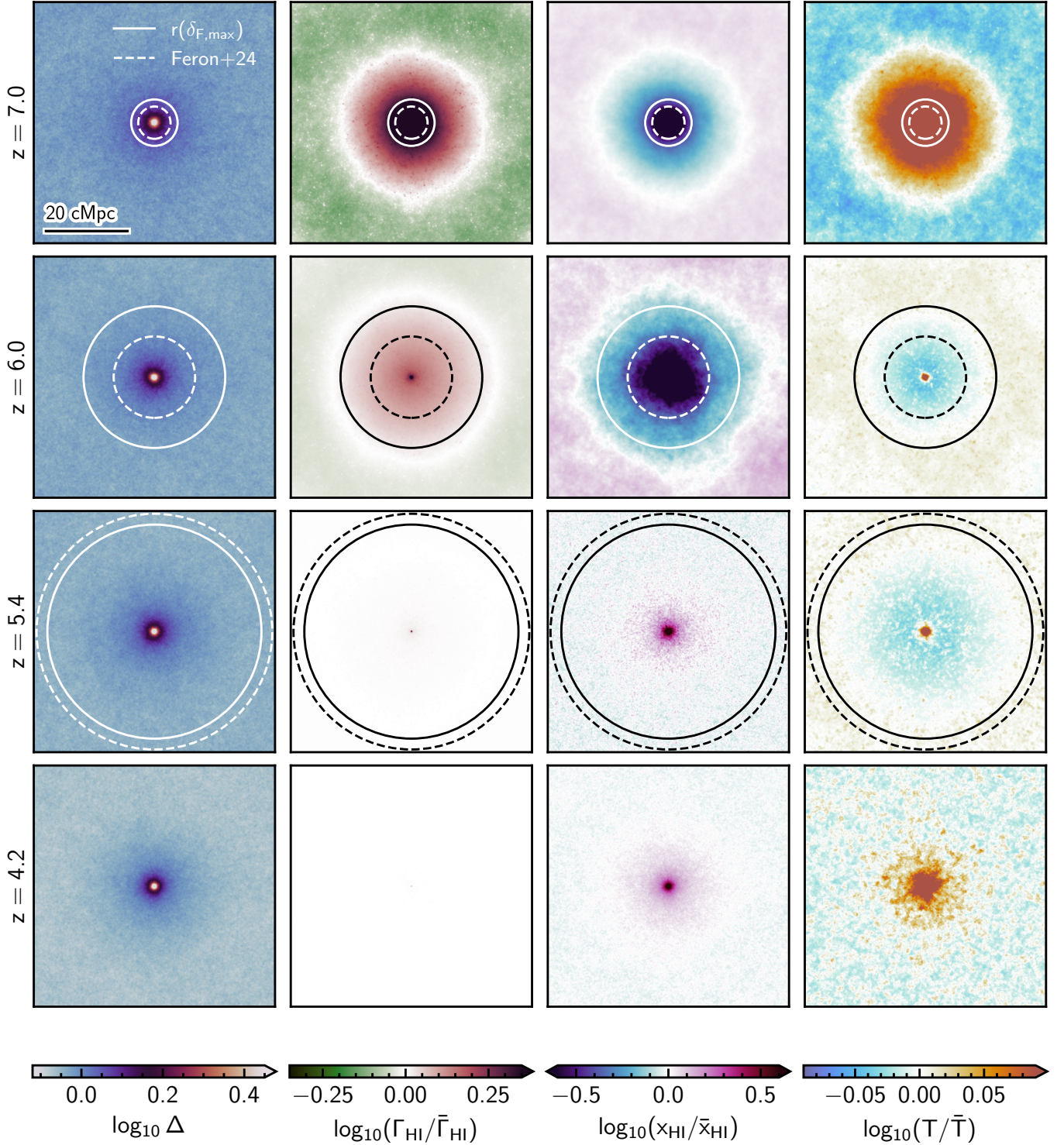


**Figure 3.** Stacked slices of the key quantities that set the real-space Ly  $\alpha$  transmission displayed in Fig. 2 (the slices used to produce the stacks are the same as those used to make Fig. 2). From left to right, the columns show the fluctuations in: gas density  $\log_{10} \Delta = \log_{10}(\rho_g/\bar{\rho}_g)$ ; hydrogen photoionisation rate  $\log_{10}(\Gamma_{\text{HI}}/\bar{\Gamma}_{\text{HI}})$ ; neutral hydrogen fraction  $\log_{10}(x_{\text{HI}}/\bar{x}_{\text{HI}})$ ; and gas temperature  $\log_{10}(T/\bar{T})$ . In each case, barred quantities indicate the global volume average of a quantity. From top to bottom, the rows display the stacks for  $z = 7, 6, 5.4$  and  $4.2$ . Note that in each case we clip the dynamic range of the colourmap, in order to centre the mean and highlight structure (the clipped end of the colourbar is triangular). As in Fig. 2, we also show the distance at which the halo–Ly  $\alpha$  transmission correlation is largest ( $r(\delta_{F,\max})$ , solid circle), and the mean free path of Lyman limit photons around haloes from Feron et al. (2024) (dashed circle).

halo with  $M_h \geq 10^{10} h^{-1} M_\odot$  in the fiducial 40-2048 simulation, by recentering the grids on the centre of mass of every halo. We stack slices to compute the average value of  $F_{\text{real}}$  in each pixel, before normalising by the global volume-averaged transmission  $\bar{F}_{\text{real}}$ .

Fig. 2 displays the normalised stacked transmission  $F_{\text{real}}/\bar{F}_{\text{real}}$  at  $z = 7, 6, 5.4$  and  $4.2$ . We show the result for the fiducial 40-2048 simulation, but note that the general features are the same for the other reionisation models (aside from differences in timing due to the different reionisation histories). At all redshifts shown in Fig. 2, there is a central region ( $\sim$  few cMpc in extent) where  $\log_{10}(F_{\text{real}}/\bar{F}_{\text{real}}) \ll 0$  (i.e. the Ly  $\alpha$  transmission is lower than average). At  $z = 7$ , this region of low transmission is followed by an annulus of excess transmission (i.e.  $\log_{10}(F_{\text{real}}/\bar{F}_{\text{real}}) > 0$ ), extending out to a radius of  $\sim 10$  cMpc. Beyond this region, the transmission again drops below the average. The picture is similar for  $z = 6$  and  $z = 5.4$ , but the central reduction in transmission is stronger, and the excess transmission begins at a larger distance from the halo, extends further, and is weaker. By  $z = 4.2$  the central region of low transmission is the only feature that is still visible in the map.

The behaviour of the transmission in Fig. 2 may be understood by examining Fig. 3, where we show averages of the key quantities used in Eq. (1), namely gas overdensity  $\Delta$ , photoionisation rate  $\Gamma_{\text{HI}}$ , neutral hydrogen fraction  $x_{\text{HI}}$  and gas temperature  $T$ .<sup>2</sup> The stacks in Fig. 3 are calculated in the same fashion as in Fig. 2. At all redshifts,  $\Delta$  is centrally concentrated with a value at  $r \gtrsim 20$  cMpc that gradually becomes smaller with time as structure formation progresses. At  $z = 7$ , the local radiation field around the haloes is clearly visible in the excess  $\Gamma_{\text{HI}}$  at  $r \lesssim 15$  cMpc. This drives a corresponding decrease in  $x_{\text{HI}}$  and excess in  $T$  due to photoionisation and photoheating, respectively (i.e., from the ionised bubbles around the sources). This is also demonstrated by the dashed circles in and Fig. 2 and Fig. 3 which show the Lyman-limit mean free path around haloes,  $\Lambda_{\text{mfp}}$ , from Feron et al. (2024).<sup>3</sup> This implies the local radiation field from ionising sources plays an important role in setting the galaxy–Ly  $\alpha$  transmission correlation. We return to discuss the solid circles in Fig. 2 and Fig. 3 in Sec. 3.3.

Toward lower redshift the fluctuations in  $\Gamma_{\text{HI}}$  fade away as the intensity of the UV background (UVB) increases, and by  $z = 5.4$  only the very central excess is visible. The effect of the diminishing UVB fluctuations are again mirrored in the behaviour of the neutral hydrogen fraction (and hence also  $F_{\text{real}}$ ). Lastly, at  $z = 4.2$  (after the end of reionisation) all the gas in the IGM is highly ionised and the central region in the stacked slice is more neutral than average due to the larger gas density (i.e.,  $x_{\text{HI}} \propto \Delta$  for gas in ionisation equilibrium).

The behaviour of the temperature fluctuations, displayed in the right column of Fig. 3, is slightly different. The central region at all redshifts contains hot gas associated with shocks from structure formation. At  $z = 7$ , the region around the stacked haloes ( $r \lesssim 15$  cMpc) is dominated by recently photoheated gas, which produces an excess in  $T$  relative to the average. By  $z = 6$ , the excess in temperature is still present, but at larger distances ( $10 \lesssim r/\text{cMpc} \lesssim 30$ ); regions further away from the sources have been more recently photoheated and have had less time to cool. Gas in the low-density IGM cools adiabatically via the expansion of the Universe and also through inverse Compton scattering off cosmic microwave background pho-

tons (an important process at these redshifts, see e.g. Puchwein et al. 2019), so the gas closer to the sources ( $1 \lesssim r/\text{cMpc} \lesssim 10$ ) is instead now cooler than average. At  $z = 5.4$  the picture is similar to  $z = 6$ , but the excess in temperature occurs still further away from sources ( $r \gtrsim 15$  cMpc). By  $z = 4.2$  the coherent radial fluctuations in temperature have largely faded, and the temperature more closely correlates with the density field (i.e., the IGM is relaxing toward a power-law temperature-density relation,  $T = T_0 \Delta^{\gamma-1}$ ). The fact that – due to the long cooling timescale for the low density IGM – relic fluctuations in temperature persist longer than the fluctuations in photo-ionisation rate will have consequences for the *post-reionisation* galaxy–Ly  $\alpha$  transmission correlation (see also D’Aloisio et al. 2018; Keating et al. 2018; Molaro et al. 2023, for related work). We will discuss this further in Sec. 4.3.

### 3 THE GALAXY–LY $\alpha$ TRANSMISSION CORRELATION IN SHERWOOD-RELICS

#### 3.1 Computing the galaxy–Ly $\alpha$ transmission correlation

We now turn to examine the galaxy–Ly  $\alpha$  transmission correlation using our mock Ly  $\alpha$  forest spectra that include redshift space effects. We do this by selecting each halo that satisfies a given mass constraint (usually  $M_h \geq 10^{10} h^{-1} M_\odot$ ) and then calculating the distance to each pixel in our Ly  $\alpha$  forest sightlines. We then use bins of width  $\Delta r = 147$  ckpc and average the transmission over many sightlines to obtain  $\langle F(r) \rangle$ . The galaxy–Ly  $\alpha$  transmission correlation is then

$$\delta_F(r) = \frac{\langle F(r) \rangle}{\bar{F}} - 1, \quad (2)$$

where  $\bar{F}$  is the global volume-averaged Ly  $\alpha$  transmission at that redshift. Throughout the remainder of this work we therefore also refer to the galaxy–Ly  $\alpha$  transmission correlation as  $\delta_F$ . For the sake of clarity, we note that  $\delta_F < 0$  corresponds to less transmission than the average, and  $\delta_F > 0$  corresponds to more.

#### 3.2 Comparison with observational data

We begin with a comparison to observational data at  $z < 4$ , well after reionisation has completed. In Fig. 4 we compare these data to  $\delta_F$  as a function of distance  $r$  from haloes with  $M_h \geq 10^{10} h^{-1} M_\odot$  in the 40-2048 and 160-2048 models at  $z \leq 5.4$ . This redshift corresponds roughly to the endpoint of reionisation in the simulations (i.e., where the volume-averaged neutral fraction  $\bar{x}_{\text{HI}} \leq 10^{-3}$ , see Table 1). In both the 40-2048 and 160-2048 runs,  $\delta_F < 0$  close to the haloes, where  $\delta_F$  decreases rapidly with decreasing distance. Furthermore, at fixed  $r$ ,  $\delta_F$  increases with decreasing redshift. For the 40-2048 run,  $\delta_F$  drops below  $-0.1$  at  $r \lesssim 5\text{--}10$  cMpc, depending on redshift, while for 160-2048 the same decrease in  $\delta_F$  occurs at  $r \lesssim 10\text{--}20$  cMpc. This decrement in  $\delta_F$  over larger distances in the 160-2048 run is due to the more massive haloes present in the larger volume, which sit in larger associated overdensities (see Fig. A1). For  $r > 20$  cMpc (50 cMpc) in the 40-2048 (160-2048) run, the transmission approaches the mean value (i.e.  $\delta_F \rightarrow 0$ ).

The shape of  $\delta_F$  predicted by the models is in qualitative agreement with observations, and where the redshift of the data points and simulations are similar ( $z \sim 4$ ) the agreement is reasonable. However, we do not expect perfect quantitative agreement between our models and observations, given that the observations are at (often much) lower redshift (the closest observations our lowest redshift output at  $z = 4.1$  are the Matthee et al. 2024 results, at  $z \approx 4$ ). In addition, we note again that the lack of a detailed subgrid model for

<sup>2</sup> Note that Fig. 3 shows averages over each quantity relevant to Eq. (1), *not* the values of each quantity that will produce the average  $F_{\text{real}}$  shown in Fig. 2.

<sup>3</sup> The halo mass bins used to calculate  $\Lambda_{\text{mfp}}$  in Feron et al. (2024) are slightly different to those employed here, with a mean halo mass  $\langle M_h/h^{-1} M_\odot \rangle$  of  $10^{10.5}$  at  $z = 7$ ,  $10^{10.7}$  at  $z = 6$  and  $10^{10.9}$  at  $z = 5.4$ .

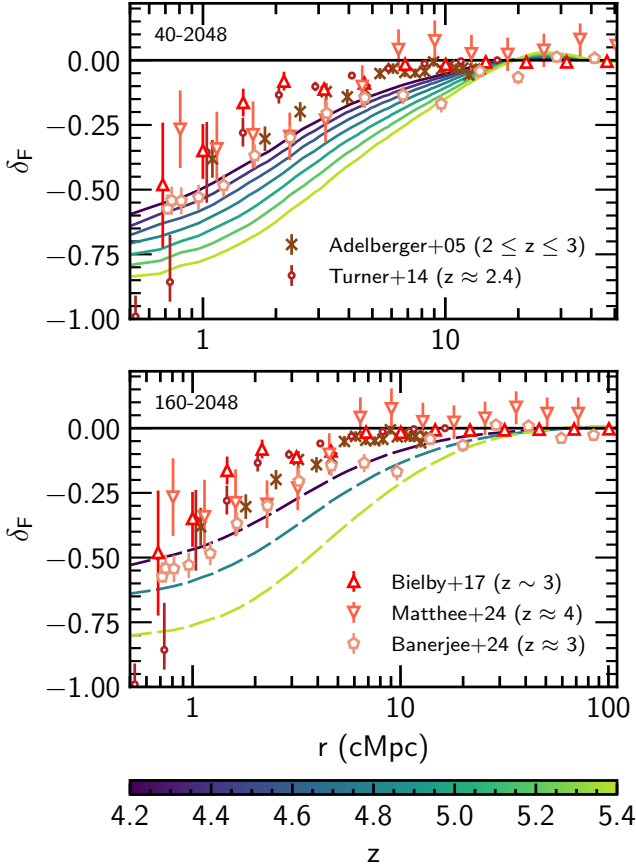


**Figure 4.** The low-redshift ( $z \leq 5.4$ ) galaxy–Ly  $\alpha$  transmission correlation ( $\delta_F$ , see Eq. (2)) as a function of distance  $r$  from haloes with mass  $M_h \geq 10^{10} h^{-1} M_\odot$  in the fiducial 40-2048 (solid, top row) and 160-2048 (dashed, bottom row) simulations. The 40-2048 model is shown every  $\Delta z = 0.2$  between  $z = 4.2$  and  $z = 5.4$ , while the 160-2048 model is shown at  $z = 4.2, 4.8$  and  $5.4$ . We also show constraints from  $2 \leq z \leq 4$  due to Adelberger et al. (2005); Turner et al. (2014); Bielby et al. (2017); Matthee et al. (2024); Banerjee et al. (2024). Note the different ranges in  $r$  between the top and bottom panels. Redshift differences between the data and simulations mean we do not expect quantitative agreement.

galaxy formation and feedback (which may be important for matching observations of  $\delta_F \ll 0$  close to galaxies, see Meiksin et al. 2017; Sorini et al. 2020) in Sherwood-Relics means that we do not expect good agreement close to ( $r \lesssim 1$  cMpc) haloes.

In Figs. 5, 6 and 7 we now focus on the data at redshifts approaching the reionisation era. We show  $\delta_F$  for  $z > 5.4$  compared to observational constraints from Meyer et al. (2019), Meyer et al. (2020) and Kashino et al. (2023), respectively. Beginning with the general features of  $\delta_F$  in our models at high  $z$ , we observe a similar rapid decrease in  $\delta_F$  close to haloes as observed at lower  $z$ , but now  $\delta_F > 0$  further away from haloes ( $r \gtrsim$  few cMpc). For both the 40-2048 and 160-2048 models, the amplitude of this excess is larger at higher  $z$ , when there is very little transmission in the IGM (i.e. the excess is not driven by a very large  $\langle F(r) \rangle$ , but rather the contrast with small  $\bar{F}$ ). As redshift decreases, the peak of the excess shifts to larger distances, from  $r \approx 6$  cMpc ( $r \approx 12$  cMpc) at  $z = 7$  for 40-2048 (160-2048) to  $r \sim 20$  cMpc at  $z = 6$  for both models, although around  $z = 6$  the “peak” becomes very broad. For  $r \gtrsim 20$  cMpc ( $r \gtrsim 60$  cMpc) at  $z \geq 6$ ,  $\delta_F$  becomes negative again in the 40-2048 (160-2048) model, due to gas in the IGM that has not yet been highly ionised.

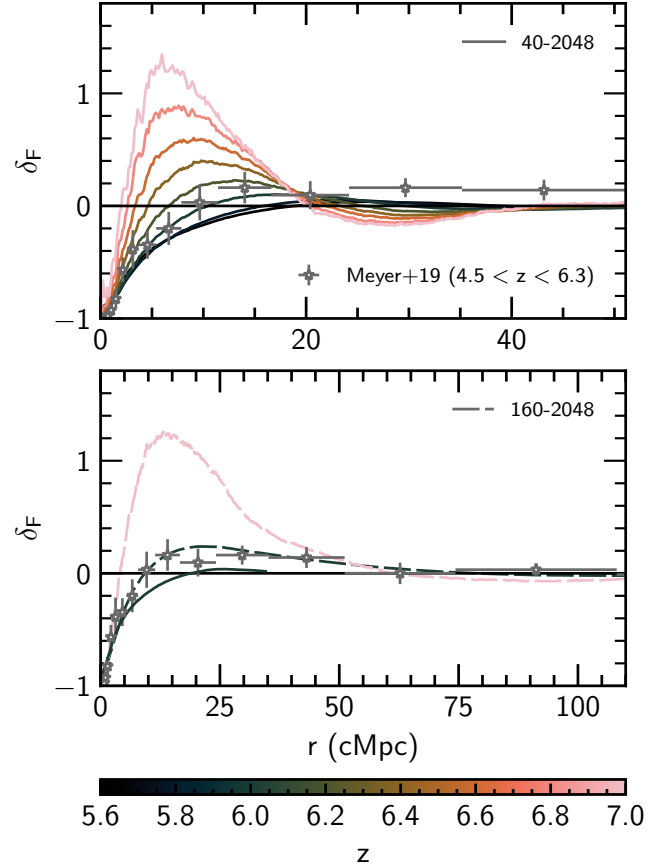


**Figure 5.** The high-redshift ( $z > 5.4$ ) galaxy–Ly  $\alpha$  transmission correlation ( $\delta_F$ , see Eq. (2)) as a function of distance  $r$  from haloes with mass  $M_h \geq 10^{10} h^{-1} M_\odot$  in the fiducial 40-2048 (solid, top and bottom rows) and 160-2048 (dashed, bottom row) simulations. The 40-2048 model is shown every  $\Delta z = 0.2$  between  $z = 5.6$  and  $z = 7.0$ , while the 160-2048 model is shown at  $z = 6.0$  and  $7.0$ . Also shown are observational constraints due to Meyer et al. (2019), calculated using C IV absorbers over the redshift range  $4.5 < z_{\text{CIV}} < 6.3$  (with mean redshift  $\langle z_{\text{CIV}} \rangle = 5.18$ ) as proxies for galaxies when computing  $\delta_F$ . As discussed in Sec. 2.2, they argue that these absorbers approximately correspond to halo masses  $M_h \gtrsim 10^{9.8} h^{-1} M_\odot$ , although note the observed C IV bias they report is uncertain and is consistent with host halo masses as large as  $M_h = 10^{12.4} h^{-1} M_\odot$ . For  $r \lesssim 20$  cMpc, we find excellent agreement ( $< 1\sigma$ ) between the Meyer et al. (2019) results and our fiducial 40-2048 model, but at  $z = 6$  as opposed to  $\langle z_{\text{CIV}} \rangle = 5.18$ . Interestingly, a qualitatively similar result was also independently noted by Garaldi et al. (2022) using the THESAN simulations, where these authors found simulation outputs at  $z \sim 6.2$  were in better agreement with the Meyer et al. (2019) data. In addition to the timing discrepancy, for  $r \gtrsim 20$  cMpc we are unable to reproduce the observed  $\delta_F > 0$  at any of the redshifts shown. For the 160-2048 model, we also find excellent agreement at  $z = 6$  (mostly  $< 1\sigma$ ) over the entire range shown (110 cMpc). Again, this redshift, at which the 160-2048 model best agrees with the data, is higher than the average redshift of C IV absorbers in the Meyer et al.

Turning now to comparing the high- $z$   $\delta_F$  in our models to observational data, we begin with Fig. 5 and the Meyer et al. (2019) constraints. Meyer et al. (2019) use the positions of C IV absorbers over the redshift range  $4.5 < z_{\text{CIV}} < 6.3$  (with mean redshift  $\langle z_{\text{CIV}} \rangle = 5.18$ ) as proxies for galaxies when computing  $\delta_F$ . As discussed in Sec. 2.2, they argue that these absorbers approximately correspond to halo masses  $M_h \gtrsim 10^{9.8} h^{-1} M_\odot$ , although note the observed C IV bias they report is uncertain and is consistent with host halo masses as large as  $M_h = 10^{12.4} h^{-1} M_\odot$ . For  $r \lesssim 20$  cMpc, we find excellent agreement ( $< 1\sigma$ ) between the Meyer et al. (2019) results and our fiducial 40-2048 model, but at  $z = 6$  as opposed to  $\langle z_{\text{CIV}} \rangle = 5.18$ . Interestingly, a qualitatively similar result was also independently noted by Garaldi et al. (2022) using the THESAN simulations, where these authors found simulation outputs at  $z \sim 6.2$  were in better agreement with the Meyer et al. (2019) data. In addition to the timing discrepancy, for  $r \gtrsim 20$  cMpc we are unable to reproduce the observed  $\delta_F > 0$  at any of the redshifts shown. For the 160-2048 model, we also find excellent agreement at  $z = 6$  (mostly  $< 1\sigma$ ) over the entire range shown (110 cMpc). Again, this redshift, at which the 160-2048 model best agrees with the data, is higher than the average redshift of C IV absorbers in the Meyer et al.



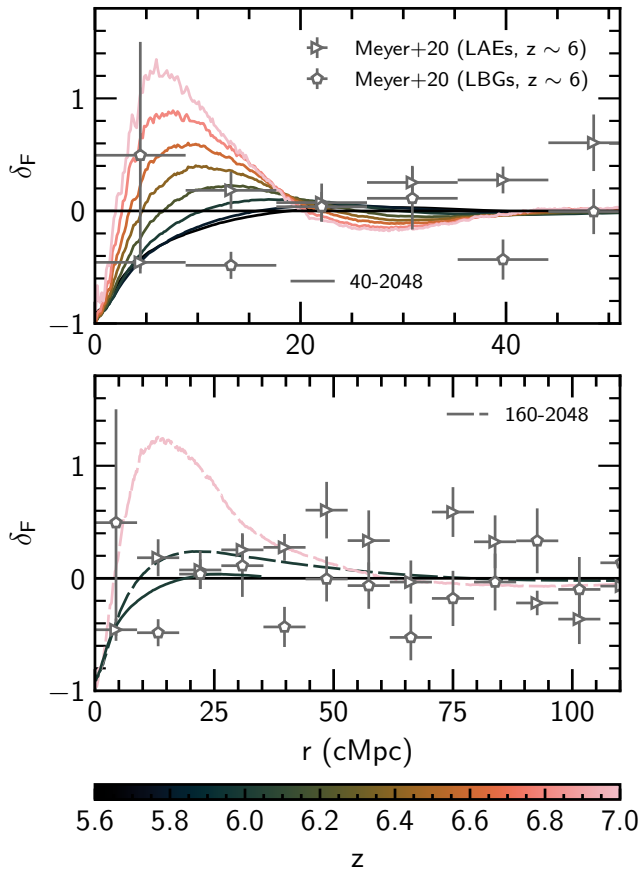


**Figure 6.** As in Fig. 5, but with constraints from Meyer et al. (2020), where  $\delta_F$  is computed for Lyman-break galaxies (LBGs, triangles) and Ly  $\alpha$  emitters (LAEs, pentagons) at  $z \sim 6$ .

(2019) dataset. This is perhaps surprising, given that our simulations are calibrated to reproduce observations of the mean transmission in the Ly  $\alpha$  forest at  $z \lesssim 6$ , but it is equivalent to requiring  $\bar{x}_{\text{HI}} \sim 0.1$  at  $z = 5.2$ . For comparison, the distribution of Ly  $\alpha$  effective optical depths at  $z \leq 5.2$  are consistent with a fully reionised IGM and a homogeneous UV background, suggesting there is little scope for delaying the end of reionisation below this redshift (Bosman et al. 2022).

We move now to Fig. 6 and the follow-up work of Meyer et al. (2020), where the cross-correlation is computed for Lyman-break galaxies (LBGs) and Ly  $\alpha$  emitters (LAEs) at  $z \sim 6$  as opposed to C IV absorbers at slightly lower redshift. In contrast to the Meyer et al. (2019) result, we find poor agreement with the Meyer et al. (2020) constraints, except for the negative  $\delta_F$  at small ( $r \lesssim 5$  cMpc) scales. Indeed, Meyer et al. (2020) note that their measurement is impacted by the small sample size and noise, and argue that the two-point cross-correlation function between transmission spikes (high signal-to-noise pixels with  $F > 0.02$ ) and galaxy positions should provide a more robust measurement. We briefly discuss this statistic in App. B, but focus on the more widely used  $\delta_F$  throughout the main portion of this work.

Next, we turn to Fig. 7 and the comparison with the Kashino et al. (2023) constraints from a single QSO field from the EIGER survey. Kashino et al. (2023) use [O III]-emitting galaxies when calculating  $\delta_F$  and, while we do not directly model [O III] emission, it has been shown that these [O III] emitters tend to reside in haloes with  $M_{\text{h}} \approx 10^{10.7} h^{-1} M_{\odot}$  (Pizzati et al. 2024, see also discussion in

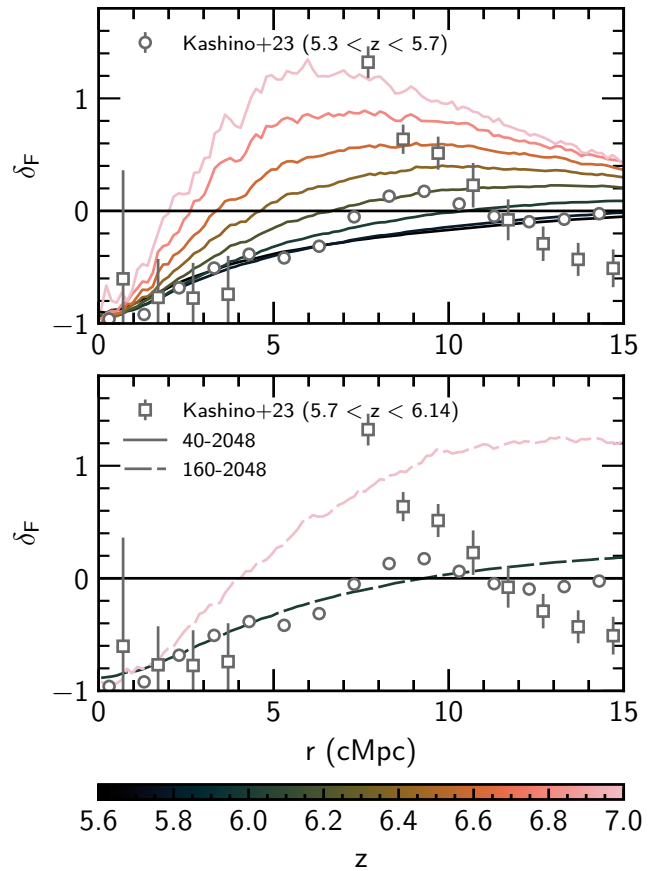


**Figure 7.** As in Fig. 5, but shown over a smaller range in  $r$  and with constraints from Kashino et al. (2023), where [O III] emitters were used in the calculation of  $\delta_F$ . In the interests of readability, the higher (lower) redshift Kashino et al. (2023) points have been offset by 0.2 (−0.2) cMpc and we do not show the full extent of the higher redshift Kashino et al. (2023) data, which extends up to  $\delta_F \approx 3$  at  $r \approx 5$  cMpc. Note that both the top and bottom panels now share the same range in  $r$ .

Sec. 2.2). For  $z \sim 7$ , we find qualitative agreement with the Kashino et al. (2023) measurement for  $r \lesssim 10$  cMpc, namely  $\delta_F < 0$  at small distances ( $r \lesssim 4$  cMpc) and a strongly-peaked excess in  $\delta_F$  at slightly larger distances ( $r \approx 6$  cMpc), but are unable to match the extreme value of  $\delta_F \approx 3$  at  $r \approx 5$  cMpc (not shown in Fig. 7, see figure caption) or the behaviour of  $\delta_F$  for  $r \gtrsim 10$  cMpc. Our analysis is consistent with the interpretation of Garaldi & Bellscheidt (2024a), who suggest that the Kashino et al. (2023) result is likely dominated by stochasticity, given that it focuses on a single QSO sightline. Future results from all six QSO fields in the EIGER survey could provide interesting new insights into the nature of the galaxy–Ly  $\alpha$  transmission correlation at high  $z$ . In the context of modelling, varying the source model in our simulations could also prove instructive, particularly for small  $r$ .

### 3.3 The galaxy–Ly $\alpha$ transmission correlation and the local mean free path around haloes

Finally, we explore the connection between the location of the peak of  $\delta_F$  in Figs. 5, 6 and 7 and the local mean free path of Lyman-limit photons around galaxies, as highlighted recently by Garaldi & Bellscheidt (2024a). In this case, we calculate  $\delta_F$  without including the effect of peculiar velocities to enable a fair comparison with the real-space Ly  $\alpha$  transmission defined in Eq. (1). We compute



the distance at which  $\delta_F$  is largest,  $r(\delta_{F,\max})$ , by first smoothing  $\delta_F$  with a moving window of eight times the bin width ( $\Delta r = 1180$  ckpc) to reduce noise (for comparison, [Garaldi & Bellscheidt 2024a](#) use a window of 2950 ckpc).

We show  $r(\delta_{F,\max})$  as a solid circle in Fig. 2 and Fig. 3. At all redshifts,  $r(\delta_{F,\max})$  occurs well away from the high-density peak associated with the haloes. At  $z = 7$  and  $z = 6$ ,  $r(\delta_{F,\max})$  sits inside the region where the radiation field is enhanced relative to the background, and the hydrogen is correspondingly more ionised. At  $z = 5.4$  however, after the radiation field becomes close to homogeneous, the (very small) peak that remains for the excess transmission approximately coincides with the residual excess in the gas temperature. The behaviour of the halo mean free path,  $\Lambda_{\text{mfp}}$ , measured from Sherwood-Relics by [Feron et al. \(2024\)](#)<sup>4</sup> (dashed circles) is qualitatively similar to that of  $r(\delta_{F,\max})$ . There will be small differences due, in part, to the slightly different sample of haloes used to calculate  $\Lambda_{\text{mfp}}$  in [Feron et al. \(2024\)](#) (see also Sec. 4.1). Nevertheless, as first noted recently by [Garaldi & Bellscheidt \(2024a\)](#), this suggests the typical scale for the excess transmission in the galaxy–Ly  $\alpha$  transmission correlation is related to the local mean free path for ionising photons around galaxies. Prior to the end of reionisation, this quantity will be larger than the mean free path in the average IGM, but following reionisation it will be smaller (see e.g., fig. 8 in [Feron et al. 2024](#) and the related discussion, as well as [Fan et al. 2025](#)).

## 4 THE DETAILED PHYSICAL ORIGIN OF THE GALAXY–LY $\alpha$ CORRELATION

### 4.1 Degeneracy between halo mass and neutral fraction

We now turn to more closely examine the various factors that influence the galaxy–Ly  $\alpha$  correlation in our simulations. First, we examine the effect of halo mass on the galaxy–Ly  $\alpha$  transmission correlation in Fig. 8. We consider the results from the 160-2048 model at  $z = 6$  and  $z = 5.4$ , although note that the general trends are the similar in the 40-2048 box. Here we use the 160-2048 box instead of the fiducial, higher-resolution 40-2048 box because it contains haloes with larger masses,  $M_h > 10^{12} h^{-1} M_\odot$  while also still resolving the minimum halo mass  $M_h = 10^9 h^{-1} M_\odot$  that hosts ionising sources in our simulations (see e.g., Fig. A1). We compute  $\delta_F$  for haloes spanning four decades in mass, although note the lowest mass bin ( $10^9 \leq M_h/h^{-1} M_\odot < 10^{10}$ ) is shown only for comparison here and is not used throughout the rest of this work. For mass bins with  $M_h \geq 10^{10} h^{-1} M_\odot$  we use all haloes when calculating  $\delta_F$  and, for computational efficiency, we draw a representative sample of  $10^4$  haloes for those with  $10^9 \leq M_h/h^{-1} M_\odot < 10^{10}$ . At  $z = 6$  ( $z = 5.4$ ) the largest halo has a mass of  $4.5 \times 10^{12} h^{-1} M_\odot$  ( $6.9 \times 10^{12} h^{-1} M_\odot$ ).

In the lower panel of Fig. 8 at  $z = 5.4$  (close to the end of reionisation), for  $r \lesssim 50$  cMpc we find that the radial extent of the region with negative  $\delta_F$  becomes larger as the halo mass increases. This is because the lower-mass haloes are associated with smaller overdensities where the clustering and infall of neutral hydrogen is weaker. In photoionisation equilibrium,  $\Delta \propto x_{\text{HI}}$ , and in the absence of a strong proximity effect or feedback we therefore expect the gas approaching the lower-mass haloes to have smaller  $x_{\text{HI}}$  (i.e., are more highly ionised) and larger transmission (i.e., a smaller region of negative  $\delta_F$ ).

The results displayed in the upper panel of Fig. 8 at  $z = 6$  are more

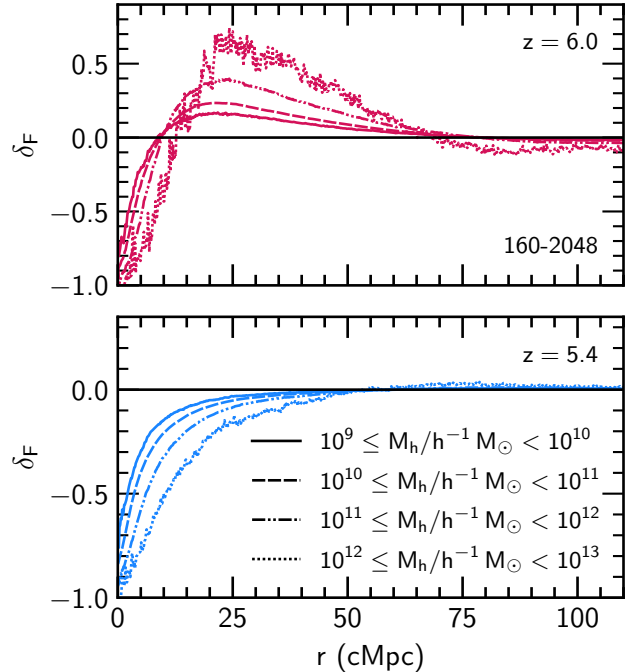


**Figure 8.** Impact of halo mass on the galaxy–Ly  $\alpha$  transmission fluctuation correlation in the 160-2048 run at  $z = 6.0$  (top, pink) and  $z = 5.4$  (bottom, blue). We show the correlation for bins spanning four decades in mass:  $10^9 \leq M_h/h^{-1} M_\odot < 10^{10}$  (solid),  $10^{10} \leq M_h/h^{-1} M_\odot < 10^{11}$  (dashed),  $10^{11} \leq M_h/h^{-1} M_\odot < 10^{12}$  (dash-dot-dotted), and  $10^{12} \leq M_h/h^{-1} M_\odot < 10^{13}$  (dotted).

complicated, however. Due to proximity to the ionising sources, the gas within  $r \lesssim 5$  cMpc is reionised earlier than gas further away (see e.g., fig. 1 in [Puchwein et al. 2023](#)). Therefore, by  $z = 6$ , this gas is already in photoionisation equilibrium and the behaviour observed at  $z = 5.4$  is replicated. However, further away from haloes ( $10 \lesssim r/\text{cMpc} \lesssim 70$ ), it is now the more massive haloes which have larger, positive  $\delta_F$  (i.e. excess transmission relative to the mean). This is because, in the Sherwood-Relics model, the ionising emissivity of a source,  $\dot{N}_\gamma$ , is proportional to halo mass ([Kulkarni et al. 2019](#)); when the IGM is optically thin to ionising photons the photoionisation rate in the low-density IGM (i.e. far away from haloes where local density effects become unimportant) is always larger around more massive haloes due to source clustering. We therefore speculate that simulations which use a different source luminosity assignment, such as a ‘Democratic’ model where  $\dot{N}_\gamma$  is independent of  $M_h$  ([Cain et al. 2023](#); [Asthana et al. 2024b](#)), may change these results. Temperature fluctuations also play a role, as gas that is ionised (and therefore heated) earlier has more time to cool than gas which is ionised later. At a given density, colder gas is more neutral (since the recombination coefficient scales as  $\alpha \propto T^{-0.72}$  for gas  $T \sim 10^4$  K) and so the (relatively) cooler gas near to haloes will also exhibit reduced transmission compared to the hotter gas further away.

In Fig. 9, we instead compare  $\delta_F$  for the three additional reionisation models listed in Table 1 to the fiducial model (solid curves in each panel). The redshift evolution of the galaxy–Ly  $\alpha$  transmission correlation is different for each reionisation model. Hence, rather than compare these models at fixed redshift, in Fig. 9 we instead compare the models at approximately the same volume averaged neutral hydrogen fraction, which in this case are the values assumed in the fiducial model at  $z = 7, 6$  and  $5.4$ . We find that each model shows similar behaviour at fixed neutral fraction, suggesting that the

<sup>4</sup> [Feron et al. \(2024\)](#) measure  $\Lambda_{\text{mfp}}$  from sightlines originating at the virial radius of haloes (see their sec. 4 for details).

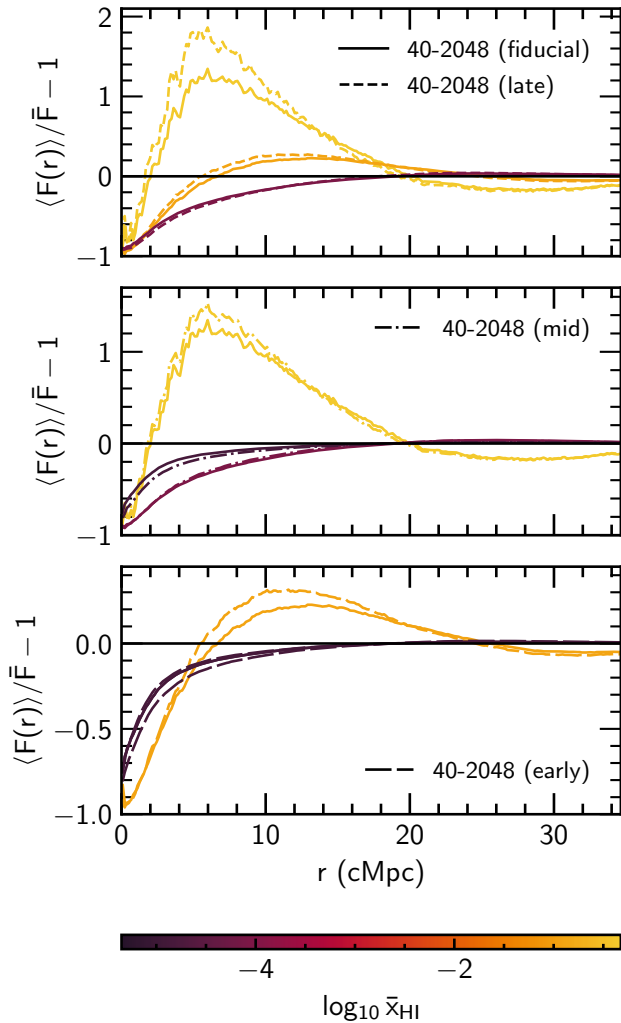


**Figure 9.** Comparison of different reionisation histories to the fiducial 40-2048 run at approximately equal volume weighed IGM neutral hydrogen fractions,  $\bar{x}_{\text{HI}}$ . Shown are the late (top panel, dashed), mid (middle panel dot-dashed) and early (bottom panel, long dashed) reionisation models along with the fiducial model (solid, with the same curves are shown in all panels). The colour indicates  $\log_{10} \bar{x}_{\text{HI}}$ . In each case we select the closest match in  $\bar{x}_{\text{HI}}$  between each of the three reionisation models to the fiducial model values measured at  $z = 7, 6$  and  $5.4$ . Note the neutral fraction decreases with decreasing redshift, so in each panel the curves with larger (smaller)  $\bar{x}_{\text{HI}}$  correspond to higher (lower) redshift outputs for each model.

shape of  $\delta_F$  is determined primarily by the neutral fraction in the IGM. This is consistent with the results of Garaldi et al. (2022), who find that comparing  $\delta_F$  at a given  $\bar{x}_{\text{HI}}$  reduces the scatter between models with different reionisation histories. We note, however, that this will be at least partly degenerate with the halo mass; a larger excess transmission is observed for either a larger volume averaged neutral hydrogen fraction, or for a larger assumed halo mass. In both cases, the IGM around the haloes hosting sources will be more highly ionised than the average IGM. It may therefore be challenging to use the galaxy–Ly  $\alpha$  transmission correlation as simple proxy for either the volume averaged neutral fraction or halo mass. Nevertheless, this degeneracy also hints at a plausible route to (at least partly) resolving the redshift / H I fraction mismatch between our simulations and the Meyer et al. (2019) measurements discussed in Sec. 3.2. The cross-correlation with larger halo masses should facilitate better agreement

with the Meyer et al. (2019) measurements at smaller volume averaged neutral fractions, yielding better agreement with the observed Ly  $\alpha$  forest effective optical depth distribution at  $z \sim 5.2$ . Note again the possibility of a larger minimum host halo mass than our fiducial assumption of  $M_{\text{h}} = 10^{10} h^{-1} M_{\odot}$  is not ruled out by the rather uncertain C IV absorber bias reported by Meyer et al. (2019). Carefully investigating this will require simulations with larger volumes that sample a representative number of high mass haloes, however; we plan to investigate this further in future work.

## 4.2 The effect of inhomogeneous reionisation

We may further tease apart the physical processes driving the specific form of  $\delta_F$  presented in this work by performing a rescaling of our simulation data, each time isolating a different physical effect. As before, all calculations are performed on the fiducial 40-2048 model, including all haloes with  $M_{\text{h}} \geq 10^{10} h^{-1} M_{\odot}$  and, unless otherwise stated, *without* including the effects of peculiar velocities, to simplify our interpretation of the results.

In Fig. 10 we show the form of  $\delta_F$  when including different physical effects at  $z = 6.0$  and  $z = 5.4$ . Starting with the dotted black curve (‘original +  $v_{\text{pec}}$ ’), when compared to the solid black curve (‘original’), this shows the effect of including peculiar velocities  $v_{\text{pec}}$  in the optical depth calculation. Note that the dotted black curves are the same as those shown in Figs. 5, 6 and 7. We find that including  $v_{\text{pec}}$  makes only a modest difference to the shape of  $\delta_F$  at both redshifts shown, and so plays a minimal role in setting the shape of the galaxy–Ly  $\alpha$  transmission correlation toward the tail-end of reionisation.

Next we turn to the blue short-dashed curve in Fig. 10 (‘ion. eq.’), which shows  $\delta_F$  calculated from sightlines where the ionic abundances have been recalculated assuming the gas is in ionisation equilibrium with the spatially inhomogeneous UV background used in the simulation. Contrasting the blue short-dashed curves with the solid black curves isolates the impact of non-equilibrium effects on  $\delta_F$ . At  $z = 5.4$ , non-equilibrium effects have no impact on  $\delta_F$ . This is not surprising, given that reionisation has ended and so the gas is already largely in ionisation equilibrium. In contrast, non-equilibrium effects play a role in modifying the shape of  $\delta_F$  at  $z = 6$ , though qualitatively the picture remains the same (i.e. the excess in  $\delta_F$  remains after enforcing ionisation equilibrium). Again, it is not surprising that non-equilibrium effects are important during reionisation, because not all of the gas will be in ionisation equilibrium. Zhu et al. (2024b) also explore the impact of assuming ionisation equilibrium on  $n_{\text{HI}}$ , finding that it leads to deviations at the few per cent level.

The green dot-dashed curve in Fig. 10 (‘ion. eq., uniform  $\tilde{\Gamma}_{\text{HI}}$ ’) also assumes ionisation equilibrium, but this time we do not use the inhomogeneous UV background from the simulation. Instead, we assume that the UV background is spatially uniform with photoionisation rate  $\tilde{\Gamma}_{\text{HI}}$ . Comparing the green dot-dashed and blue short-dashed curves therefore highlights the importance of UV background fluctuations due to patchy reionisation. For  $\tilde{\Gamma}_{\text{HI}}$  we use the time-varying, average photoionisation rate measured at a distance of 1.5 cMpc away from all haloes with  $M_{\text{h}} \geq 10^{10} h^{-1} M_{\odot}$  in the fiducial 40-2048 simulation. The exact value of  $\tilde{\Gamma}_{\text{HI}}$ , or the distance at which it is measured, is of little import – the key point is that  $\tilde{\Gamma}_{\text{HI}}$  must be large enough to induce small enough equilibrium values of  $x_{\text{HI}}$  to allow for Ly  $\alpha$  transmission at  $z = 6$  ( $z = 5.4$ )  $\tilde{\Gamma}_{\text{HI}} = 2.0 \times 10^{-13} \text{ s}^{-1}$  ( $3.2 \times 10^{-13} \text{ s}^{-1}$ ). At  $z = 6$ , the effect of the uniform UVB is striking. The large excess in  $\delta_F$  around  $10 \lesssim r/\text{cMpc} \lesssim 25$  is no longer present. Instead, the  $z = 6$  green dot-dashed curve most closely resembles its post-reionisation counterpart at  $z = 5.4$ , where the shape

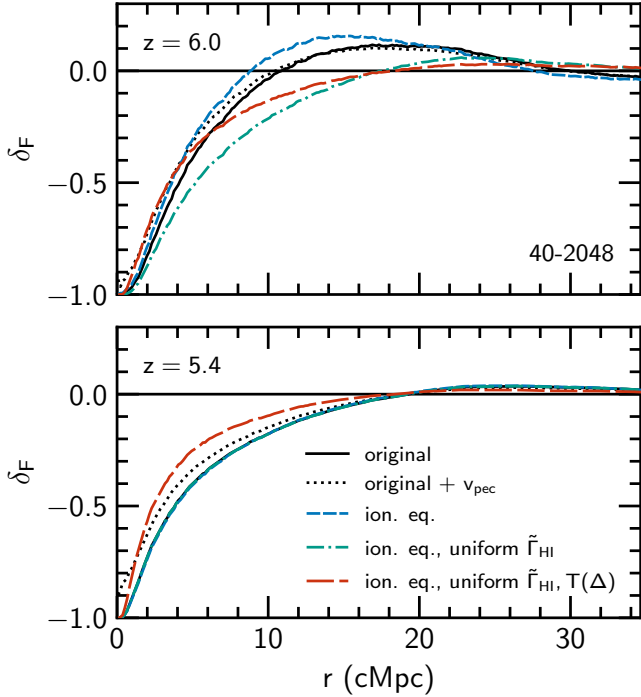


**Figure 10.** Galaxy–Ly  $\alpha$  transmission correlation calculated from the 40-2048 run (‘original’, black solid), after: recomputing the ionisation fractions of hydrogen and helium assuming ionisation equilibrium (‘ion. eq.’, blue short dashed); setting the photoionisation rate to be uniform (‘ion. eq., uniform  $\tilde{\Gamma}_{\text{HI}}$ ’, green dot-dashed); and after removing temperature fluctuations by setting  $T \propto \Delta^{\gamma-1}$  and rescaling the neutral fraction appropriately (‘ion. eq., uniform  $\tilde{\Gamma}_{\text{HI}}$ ,  $T(\Delta)$ ’, red long dashed). Also shown is the original case including peculiar velocities (‘original +  $v_{\text{pec}}$ ’, black dotted) – all other curves do not include the effect of peculiar velocities on Ly  $\alpha$  transmission. We show results at  $z = 6$  (top panel) and  $z = 5.4$  (bottom panel). Note that at  $z = 5.4$  the curves lie directly on top of one another, except for the ‘original +  $v_{\text{pec}}$ ’ and ‘ion. eq., uniform  $\tilde{\Gamma}_{\text{HI}}$ ,  $T(\Delta)$ ’ cases.

of  $\delta_F$  is characterised by  $\delta_F < 0$  for  $r \lesssim 20$  cMpc. From this, we infer that the excess in  $\delta_F$  present in the original simulation is a direct consequence of the inhomogeneous nature of reionisation, i.e. the excess is driven by local ionisation enhancement due to ionising sources, or clustered sources. This also highlights the importance of contrast with  $\delta_F$  – if  $\bar{F}$  is small (e.g., due to large neutral fractions in the average IGM) then even a small increase in transmission can lead to a large excess in  $\delta_F$ . At  $z = 5.4$ , enforcing a uniform UV background makes no difference to  $\delta_F$ , as the radiation field is already almost entirely uniform (cf. the fluctuations in  $\Gamma_{\text{HI}}$  in Fig. 3).

Finally, we turn to the red long-dashed curve in Fig. 10 (‘ion. eq., uniform  $\tilde{\Gamma}_{\text{HI}}$ ,  $T(\Delta)$ ’), which examines the effect of temperature fluctuations on  $\delta_F$ . To do this, we take the sightlines with a uniform UV background (i.e. the sightlines used to produce the green dot-dashed curve) and fit the relation

$$T = T_0 \Delta^{\gamma-1} \quad (3)$$

to the low-density ( $\Delta < 10$ ) ionised ( $x_{\text{HI}} < 10^{-3}$ ) gas at each  $z$ . To remove any effect due to the redshift evolution of  $T_0$  and  $\gamma$ , we fix their value to the average of the  $z = 6$  and  $z = 5.4$  values, taking  $T_0 = 1.14 \times 10^4$  K and  $\gamma = 1.15$ . These parameter values are consistent with the Gaikwad et al. (2020) constraints, which cover almost exactly the same redshift range. We then recalculate the temperature in every pixel using Eq. (3) and the fitted parameters  $T_0$  and  $\gamma$ , thus removing spatial fluctuations in temperature due to inhomogeneous

reionisation. The corresponding original neutral fraction  $x_{\text{HI,orig}}$  in each pixel is then rescaled, using the original temperature  $T_{\text{orig}}$  and assuming photoionisation equilibrium, according to

$$x_{\text{HI},T(\Delta)} = x_{\text{HI,orig}} \frac{\alpha_A[T(\Delta)]}{\alpha_A(T_{\text{orig}})}, \quad (4)$$

where  $\alpha_A$  is the case-A recombination rate calculated using the fit in Verner & Ferland (1996). At both redshifts, we see that removing temperature fluctuations (red long dashed curves) makes  $\delta_F$  larger (less negative) closer to haloes ( $r \lesssim 15$  cMpc) compared to the case with a uniform UV background and temperature fluctuations (green dot-dashed curves). This is because, in the patchy reionisation scenario, gas close to haloes is heated earlier than gas farther away, and therefore has more time to cool (cf. right column of Fig. 3). Setting  $T \propto \Delta^{\gamma-1}$  and performing the appropriate rescaling of  $x_{\text{HI}}$  removes these fluctuations and thus reduces the contrast between small  $r$  (where gas was initially slightly colder) and large  $r$  (where gas was initially slightly warmer), leading to the relative increase in  $\delta_F$  at small  $r$ . In the lower panel of Fig. 10 we observe this effect persists after fluctuations in the UV background have faded away (see also Christenson et al. 2023; Gangolli et al. 2024; Garaldi & Bellscheidt 2024b, for the importance of this effect in the context of the connection between Ly  $\alpha$  opacity and galaxy density).

### 4.3 Relic post-reionisation temperature fluctuations

Finally, we explore in more detail how temperature fluctuations affect the post-reionisation evolution of  $\delta_F$  at  $4.2 \leq z \leq 5.2$ . To isolate the temperature fluctuations we use the average  $T_0$  and  $\gamma$  in the models over this redshift range to once again remove any effect due to the redshift evolution of these parameters. We use  $T_0 = 1.14 \times 10^4$  K and  $\gamma = 1.25$ ; this  $\gamma$  is consistent with the Boera et al. (2019) results but  $T_0$  is somewhat larger than that reported in that study.

In Fig. 11, we show the post-reionisation evolution of  $\delta_F$  with (solid curves) and without (dashed curves) the post reionisation temperature fluctuations, focusing on the region close to the haloes where excess absorption (negative  $\delta_F$ ) occurs. The redshift evolution of the excess absorption in the original case is much stronger than in the rescaled  $T(\Delta)$  case, where the evolution now instead driven almost entirely by the redshift evolution of the mean transmission. Therefore, at these post-reionisation redshifts, we expect that relic temperature fluctuations due to inhomogeneous reionisation should play a significant role in setting the galaxy–Ly  $\alpha$  transmission correlation in proximity to the haloes hosting ionising sources. As redshift decreases, the role of temperature fluctuations diminishes (i.e. the original case approaches the  $T(\Delta)$  case). This is in line with predictions from previous studies which have found that the effect of relic temperature fluctuations (due to inhomogeneous reionisation) on e.g., the 1D Ly  $\alpha$  forest power spectrum decrease with decreasing redshift (e.g., Molaro et al. 2022). Recent work by Matthee et al. (2024) has begun to probe the excess small-scale Ly  $\alpha$  absorption around galaxies in the post-reionisation epoch ( $z \approx 4$ ). Extending this work to study the redshift evolution of this excess absorption could therefore provide insights into the nature of post-reionisation relic temperature fluctuations, and consequently on the timing of reionisation.

## 5 CONCLUSIONS

In this work, we have explored the cross-correlation between galaxies and Ly  $\alpha$  transmission in the intergalactic medium, using the

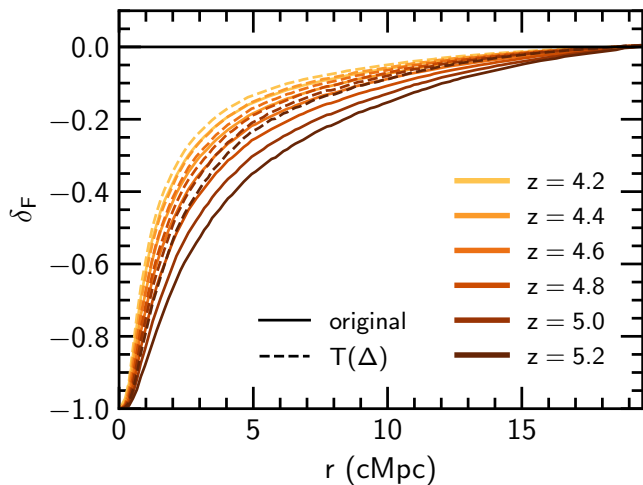


**Figure 11.** Post-reionisation galaxy–Ly  $\alpha$  transmission correlation from the original slightlines (‘original’, solid) and where temperatures have been recalculated according to  $T \propto \Delta^{\gamma-1}$  to remove spatial fluctuations in the gas temperature and  $x_{\text{HI}}$  has been appropriately rescaled (‘ $T(\Delta)$ ’, dashed), shown from  $z = 5.2$  (dark brown) to  $z = 4.2$  (gold).

Sherwood-Relics simulations (Puchwein et al. 2023). The Sherwood-Relics suite uses a novel hybrid radiative transfer approach, which self-consistently captures the hydrodynamic response of gas to inhomogeneous reionisation, and is designed to accurately model the Ly  $\alpha$  forest. Our main findings are as follows:

- We find quantitative agreement between the galaxy–Ly  $\alpha$  transmission correlation predicted by Sherwood-Relics model and Meyer et al. (2019) (who use C IV absorbers as a proxy for galaxies) if the galaxies are hosted in haloes with masses  $M_h \geq 10^{10} h^{-1} M_\odot$ , although only if there is a redshift mismatch between simulation and observation; the agreement occurs for higher redshifts in our models,  $z = 6$ , than the average redshift of  $z = 5.2$  in the Meyer et al. (2019) measurements (see also Garaldi et al. 2022, for a similar result). However, this redshift mismatch is equivalent to requiring  $\bar{x}_{\text{HI}} \sim 0.1$  at  $z \approx 5.2$ , which is inconsistent with the observed Ly  $\alpha$  forest effective optical depth distribution at  $z = 5.2$  (Bosman et al. 2022). We speculate this apparent tension may be partly resolved if the minimum C IV absorber host halo mass is instead larger than  $M_h = 10^{10} h^{-1} M_\odot$ , which is still consistent with the C IV bias reported by Meyer et al. (2019). We find poorer agreement with Meyer et al. (2020) and Kashino et al. (2023), although these measurements are more heavily impacted by limited sample size and noise.

- We also find qualitative agreement between the shape of the galaxy–Ly  $\alpha$  transmission correlation in the Sherwood-Relics models and a variety of measurements of the galaxy–Ly  $\alpha$  transmission correlation at  $z \leq 4$ . However, we are unable to perform a direct comparison as our simulation outputs do not extend below  $z = 4$ .

- The galaxy–Ly  $\alpha$  transmission correlation is sensitive to the volume averaged neutral fraction of the IGM, and is largely insensitive to different reionisation histories after accounting for differences in the neutral fraction (at least for the source model used in Sherwood-Relics, which assumes ionising luminosity is proportional to halo mass). However, the correlation is also partly degenerate with the assumed halo masses hosting the galaxies. This degeneracy means it may require an independent measure of the

host halo masses to use the galaxy–Ly  $\alpha$  transmission correlation as a simple proxy for the IGM neutral fraction.

- During reionisation, excess transmission around galaxies is driven largely by the enhanced ionising radiation field due to clustered ionising sources. Spatial fluctuations in the IGM also play a small role, due to the hotter gas present in recently reionised regions. Non-equilibrium effects only have a modest impact on the galaxy–Ly  $\alpha$  transmission correlation (see e.g., Zhu et al. 2024b). The distance where the peak excess transmission in the cross-correlation occurs is closely related to the the mean free path of Lyman-limit photons around the galaxy host haloes (see also Feron et al. 2024; Fan et al. 2025; Garaldi & Bellscheidt 2024a).

- After reionisation, for  $r \lesssim 20$  cMpc, relic spatial fluctuations in the IGM temperature affect the shape of the galaxy–Ly  $\alpha$  transmission correlation. As redshift decreases, the strength of this effect decreases, and it should fade by  $z \approx 4$  (e.g., Molaro et al. 2022). The physical explanation is that gas close to haloes is reionised earlier, and thus has more time to cool, in contrast to gas at larger distances which is reionised later and is comparatively hotter. Observations are beginning to probe the galaxy–Ly  $\alpha$  transmission correlation at  $4 \lesssim z \lesssim 5$  (Matthee et al. 2024). Constraining the redshift evolution of the correlation over this period, at scales of a  $\sim$  few cMpc, could provide complementary insight into the timing of reionisation via the signature of post-reionisation temperature fluctuations.

In summary, the galaxy–Ly  $\alpha$  transmission correlation is an exciting probe of the connection between high-redshift galaxies and the intergalactic medium, with the potential to offer new insights into the timing and main drivers of reionisation. At present, the high-redshift picture is limited by a paucity of data, but current – e.g., the *JWST* surveys EIGER (Kashino et al. 2023) and ASPIRE (Jin et al. 2024) – and future observing programmes will shed more light on this promising probe of the tail end of reionisation. Additional work on forward modelling of simulations to better reflect the observations (e.g. for the galaxy selection criteria) could prove fruitful (Garaldi & Bellscheidt 2024b). We also suggest that further modelling that explores the impact of different source models (particularly where the relationship between halo mass and ionising emissivity is varied, e.g., Cain et al. 2023; Asthana et al. 2024b, but see also Garaldi et al. 2022; Garaldi & Bellscheidt 2024a) will be especially useful in linking the properties of ionising sources with the intergalactic medium. Finally, larger volume simulations ( $> 160^3 h^{-3}$  cMpc $^3$ ) with sufficient mass resolution to resolve the Ly  $\alpha$  forest transmission at  $z > 5$  will also be valuable for exploring the galaxy–Ly  $\alpha$  correlation on large scales and for galaxy host halo masses  $M_h > 10^{12} h^{-1} M_\odot$ .

## ACKNOWLEDGEMENTS

We thank Enrico Garaldi, Daichi Kashino and Romain Meyer for insightful discussions and sharing data. The simulations used in this work were performed using the Joliot Curie supercomputer at the Trés Grand Centre de Calcul (TGCC) and the Cambridge Service for Data Driven Discovery (CSD3), part of which is operated by the University of Cambridge Research Computing on behalf of the STFC DiRAC HPC Facility (www.dirac.ac.uk). We acknowledge the Partnership for Advanced Computing in Europe (PRACE) for awarding us time on Joliot Curie in the 16th call. The DiRAC component of CSD3 was funded by BEIS capital funding via STFC capital grants ST/P002307/1 and ST/R002452/1 and STFC operations grant ST/R00689X/1. This work also used the



DiRAC@Durham facility managed by the Institute for Computational Cosmology on behalf of the STFC DiRAC HPC Facility. The equipment was funded by BEIS capital funding via STFC capital grants ST/P002293/1 and ST/R002371/1, Durham University and STFC operations grant ST/R000832/1. DiRAC is part of the National e-Infrastructure. LC and JSB are supported by STFC consolidated grant ST/X000982/1. Support by ERC Advanced Grant 320596 ‘The Emergence of Structure During the Epoch of Reionization’ is gratefully acknowledged. MGH has been supported by STFC consolidated grants ST/N000927/1 and ST/S000623/1. We thank Volker Springel for making P-Gadget-3 available. We also thank Dominique Aubert for sharing the ATON code, and Philip Parry for technical support. This work made use of the following open-source software packages: CMASHER (van der Velden 2020); MATPLOTLIB (Hunter 2007); NUMPY (Harris et al. 2020); OPEN-CV (Bradski 2000); and SCIPY (Virtanen et al. 2020). For the purpose of open access, the author has applied a Creative Commons Attribution (CC BY) licence to any Author Accepted Manuscript version arising from this submission.

## DATA AVAILABILITY

All data and analysis code used in this work are available from the first author on reasonable request. Further guidance on accessing the Sherwood-Relics simulation data may also be found at <https://www.nottingham.ac.uk/astronomy/sherwood-relics/>.

## REFERENCES

- Adelberger K. L., Shapley A. E., Steidel C. C., Pettini M., Erb D. K., Reddy N. A., 2005, *ApJ*, 629, 636
- Arrabal Haro P., et al., 2023, *Nature*, 622, 707
- Asthana S., Haehnelt M. G., Kulkarni G., Bolton J. S., Gaikwad P., Keating L. C., Puchwein E., 2024a, *arXiv e-prints*, p. arXiv:2409.15453
- Asthana S., Haehnelt M. G., Kulkarni G., Aubert D., Bolton J. S., Keating L. C., 2024b, *MNRAS*, 533, 2843
- Atek H., et al., 2024, *Nature*, 626, 975
- Aubert D., Teyssier R., 2008, *MNRAS*, 387, 295
- Bañados E., et al., 2018, *Nature*, 553, 473
- Banerjee E., et al., 2024, *arXiv e-prints*, p. arXiv:2411.11959
- Becker G. D., D’Aloisio A., Christenson H. M., Zhu Y., Worseck G., Bolton J. S., 2021, *MNRAS*, 508, 1853
- Becker G. D., Bolton J. S., Zhu Y., Hashemi S., 2024, *MNRAS*, 533, 1525
- Begley R., et al., 2024, *arXiv e-prints*, p. arXiv:2410.10988
- Bielby R. M., et al., 2017, *MNRAS*, 471, 2174
- Boera E., Becker G. D., Bolton J. S., Nasir F., 2019, *ApJ*, 872, 101
- Bosman S. E. I., Fan X., Jiang L., Reed S., Matsuoka Y., Becker G., Haehnelt M., 2018, *MNRAS*, 479, 1055
- Bosman S. E. I., et al., 2022, *MNRAS*, 514, 55
- Bradski G., 2000, Dr. Dobb’s Journal of Software Tools
- Cain C., D’Aloisio A., Gangolli N., McQuinn M., 2023, *MNRAS*, 522, 2047
- Castellano M., et al., 2024, *ApJ*, 972, 143
- Christenson H. M., et al., 2023, *ApJ*, 955, 138
- D’Aloisio A., McQuinn M., Davies F. B., Furlanetto S. R., 2018, *MNRAS*, 473, 560
- Davies F. B., et al., 2018, *ApJ*, 864, 142
- Davis M., Peebles P. J. E., 1983, *ApJ*, 267, 465
- Đurovičková D., et al., 2024, *ApJ*, 969, 162
- Eilers A.-C., Davies F. B., Hennawi J. F., 2018, *ApJ*, 864, 53
- Fan J., Chen H., Avestruz C., Khadir A., 2025, *ApJ*, 979, 150
- Feron J., Conaboy L., Bolton J. S., Chapman E., Haehnelt M. G., Keating L. C., Kulkarni G., Puchwein E., 2024, *MNRAS*, 532, 2401
- Gaikwad P., et al., 2020, *MNRAS*, 494, 5091
- Gaikwad P., et al., 2023, *MNRAS*, 525, 4093
- Gangolli N., D’Aloisio A., Cain C., Becker G. D., Christenson H., 2024, *arXiv e-prints*, p. arXiv:2408.08358
- Garaldi E., Bellscheidt V., 2024a, *arXiv e-prints*, p. arXiv:2410.02850
- Garaldi E., Bellscheidt V., 2024b, *arXiv e-prints*, p. arXiv:2410.02853
- Garaldi E., Gnedin N. Y., Madau P., 2019, *ApJ*, 876, 31
- Garaldi E., Kannan R., Smith A., Springel V., Pakmor R., Vogelsberger M., Hernquist L., 2022, *MNRAS*, 512, 4909
- Gazagnes S., et al., 2024, *arXiv e-prints*, p. arXiv:2410.03337
- Gnedin N. Y., 2014, *ApJ*, 793, 29
- Grazian A., et al., 2024, *ApJ*, 974, 84
- Greig B., Mesinger A., Bañados E., 2019, *MNRAS*, 484, 5094
- Gunn J. E., Peterson B. A., 1965, *ApJ*, 142, 1633
- Harikane Y., et al., 2023, *ApJ*, 959, 39
- Harikane Y., Nakajima K., Ouchi M., Umeda H., Isobe Y., Ono Y., Xu Y., Zhang Y., 2024, *ApJ*, 960, 56
- Harris C. R., et al., 2020, *Nature*, 585, 357
- Hunter J. D., 2007, *Computing in Science and Engineering*, 9, 90
- Jenkins A., Frenk C. S., White S. D. M., Colberg J. M., Cole S., Evrard A. E., Couchman H. M. P., Yoshida N., 2001, *MNRAS*, 321, 372
- Jin X., et al., 2023, *ApJ*, 942, 59
- Jin X., et al., 2024, *ApJ*, 976, 93
- Jung I., et al., 2020, *ApJ*, 904, 144
- Kakiichi K., et al., 2018, *MNRAS*, 479, 43
- Kannan R., Garaldi E., Smith A., Pakmor R., Springel V., Vogelsberger M., Hernquist L., 2022, *MNRAS*, 511, 4005
- Kashino D., Lilly S. J., Matthee J., Eilers A.-C., Mackenzie R., Bordoloi R., Simcoe R. A., 2023, *ApJ*, 950, 66
- Keating L. C., Puchwein E., Haehnelt M. G., 2018, *MNRAS*, 477, 5501
- Keating L. C., Weinberger L. H., Kulkarni G., Haehnelt M. G., Chardin J., Aubert D., 2020a, *MNRAS*, 491, 1736
- Keating L. C., Kulkarni G., Haehnelt M. G., Chardin J., Aubert D., 2020b, *MNRAS*, 497, 906
- Kulkarni G., Hennawi J. F., Oñorbe J., Rorai A., Springel V., 2015, *ApJ*, 812, 30
- Kulkarni G., Keating L. C., Haehnelt M. G., Bosman S. E. I., Puchwein E., Chardin J., Aubert D., 2019, *MNRAS*, 485, L24
- Madau P., Giallongo E., Grazian A., Haardt F., 2024, *ApJ*, 971, 75
- Maiolino R., et al., 2024, *A&A*, 691, A145
- Matthee J., et al., 2024, *MNRAS*, 529, 2794
- Meiksin A., Bolton J. S., Puchwein E., 2017, *MNRAS*, 468, 1893
- Meyer R. A., Bosman S. E. I., Kakiichi K., Ellis R. S., 2019, *MNRAS*, 483, 19
- Meyer R. A., et al., 2020, *MNRAS*, 494, 1560
- Molaro M., et al., 2022, *MNRAS*, 509, 6119
- Molaro M., Iršič V., Bolton J. S., Lieu M., Keating L. C., Puchwein E., Haehnelt M. G., Viel M., 2023, *MNRAS*, 521, 1489
- Naidu R. P., et al., 2022, *ApJ*, 940, L14
- Nasir F., D’Aloisio A., 2020, *MNRAS*, 494, 3080
- Pizzati E., et al., 2024, *MNRAS*, 534, 3155
- Planck Collaboration et al., 2014, *A&A*, 571, A16
- Planck Collaboration et al., 2020, *A&A*, 641, A6
- Puchwein E., Haardt F., Haehnelt M. G., Madau P., 2019, *MNRAS*, 485, 47
- Puchwein E., et al., 2023, *MNRAS*, 519, 6162
- Satyavolu S., Kulkarni G., Keating L. C., Haehnelt M. G., 2024, *MNRAS*, 533, 676
- Saxena A., et al., 2024, *A&A*, 684, A84
- Schaye J., et al., 2023, *MNRAS*, 526, 4978
- Simmonds C., et al., 2024, *MNRAS*, 527, 6139
- Smith A., Kannan R., Garaldi E., Vogelsberger M., Pakmor R., Springel V., Hernquist L., 2022, *MNRAS*, 512, 3243
- Sorini D., Davé R., Anglés-Alcázar D., 2020, *MNRAS*, 499, 2760
- Spina B., Bosman S. E. I., Davies F. B., Gaikwad P., Zhu Y., 2024, *A&A*, 688, L26
- Springel V., 2005, *MNRAS*, 364, 1105
- Tepper-García T., 2006, *MNRAS*, 369, 2025
- Tummuangpak P., Bielby R. M., Shanks T., Theuns T., Crighton N. H. M., Francke H., Infante L., 2014, *MNRAS*, 442, 2094

Turner M. L., Schaye J., Steidel C. C., Rudie G. C., Strom A. L., 2014, *MNRAS*, 445, 794  
 Umeda H., Ouchi M., Nakajima K., Harikane Y., Ono Y., Xu Y., Isobe Y., Zhang Y., 2024, *ApJ*, 971, 124  
 Verner D. A., Ferland G. J., 1996, *ApJS*, 103, 467  
 Viel M., Haehnelt M. G., Springel V., 2004, *MNRAS*, 354, 684  
 Virtanen P., et al., 2020, *Nature Methods*, 17, 261  
 Zavala J. A., et al., 2024, *Nature Astronomy*  
 Zhu Y., et al., 2023, *ApJ*, 955, 115  
 Zhu Y., et al., 2024a, *MNRAS*, 533, L49  
 Zhu H., Gnedin N. Y., Avestruz C., 2024b, *ApJ*, 975, 115  
 van der Velden E., 2020, *The Journal of Open Source Software*, 5, 2004

## APPENDIX A: RESOLUTION CONVERGENCE

Fig. A1 shows the halo multiplicity function (e.g., Jenkins et al. 2001)

$$f(\sigma, z) \frac{d \ln \sigma^{-1}}{d \ln M} = \frac{M^2}{\bar{\rho}_m(z)} \frac{dn(M, z)}{dM}, \quad (\text{A1})$$

where  $M$  is halo mass,  $\bar{\rho}_m(z)$  is the background matter density at redshift  $z$  and  $dn(M, z)/dM$  is the differential halo mass function, for the 40-512, 40-2048 and 160-2048 runs (top panel).<sup>5</sup> In the same figure, we also show the ratio of  $dn/dM$  for 40-2048, 40-1024 and 160-2048 to 40-512 (bottom panel), demonstrating – for  $10^9 \leq M_h/h^{-1} M_\odot \leq 10^{11}$  – convergence to better than 20 per cent (and mostly better than 10 per cent) for all  $z$  with respect to both box size and mass resolution. The smaller volume of the  $40 h^{-1}$  Mpc runs means that haloes with  $M_h > 10^{11} h^{-1} M_\odot$  are rarer than in the  $160 h^{-1}$  Mpc run and, above this mass, the mass functions are clearly not converged with box size or resolution. When making comparisons between runs, we therefore restrict ourselves to haloes with masses  $10^{10} \leq M_h/h^{-1} M_\odot \leq 10^{11}$ .

In Fig. A2 we show  $\delta_F$  for the  $40 h^{-1}$  Mpc Sherwood-Relics realisation at three mass resolutions, where the 40-1024 (40-512) run has a particle mass 8 (64) times larger than the 40-2048 run. We compare the three runs at approximately equal volume-averaged neutral fraction  $\bar{x}_{\text{HI}}$  to eliminate any differences due to slightly different reionisation histories. We also note that each run is normalised to the global Ly  $\alpha$  transmission for that run, which is in general different between runs. We find that the form of  $\delta_F$  for our fiducial 40-2048 model is broadly converged with mass resolution.

## APPENDIX B: GALAXY-TRANSMISSION SPIKE TWO-POINT CROSS-CORRELATION

At high redshifts ( $z \gtrsim 6$ ), the transmission in the Ly  $\alpha$  forest decreases to such a degree (see Fig. 1) that it approaches the noise level of spectrographs ( $F \sim 0.02$ , see e.g., fig. 8 in Meyer et al. 2020), making measuring  $\delta_F$  an increasingly difficult task. Meyer et al. (2020) therefore proposed using a slightly different statistic, instead measuring the two-point cross-correlation function (2PCCF) of galaxies and Ly  $\alpha$  transmission spikes. However, what constitutes a transmission spike will depend on many factors, such as the redshift at which the transmission is measured, or the resolution and noise level of the instrument being used. These complications mean we have opted to use  $\delta_F$  in our main analysis, as it can be applied more

<sup>5</sup> Strictly, the quantity shown is not the halo multiplicity function, but is a closely related function, which we plot to reduce the large dynamic range in  $dn/dM$ .

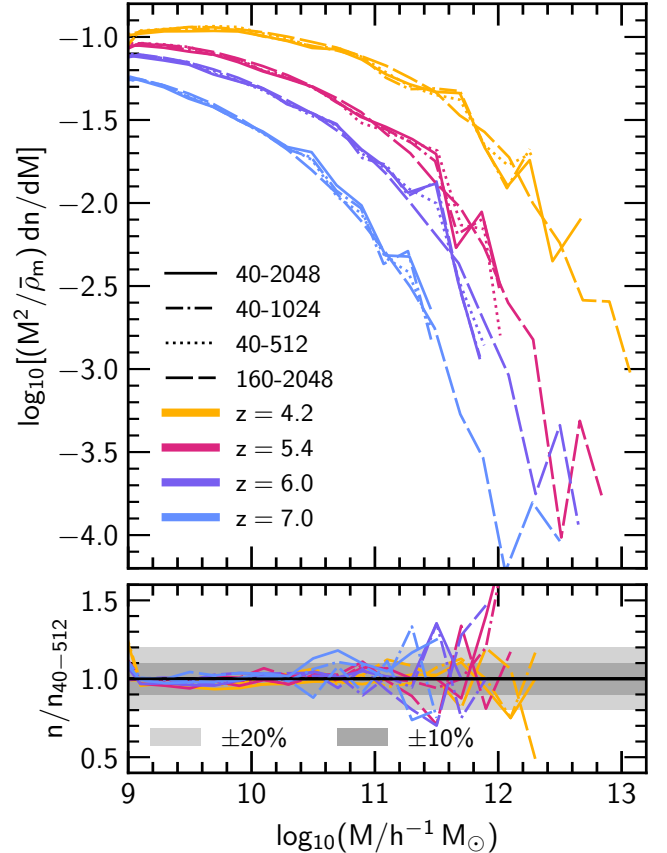


**Figure A1.** Top: halo multiplicity functions for the 40-2048 (solid), 40-1024 (dot-dashed), 40-512 (dotted), and 160-2048 (long-dashed) runs, at  $z = 7.0$  (blue),  $z = 6.0$  (purple),  $z = 5.4$  (dark pink) and  $z = 4.2$  (gold). Bottom: the ratio of 40-2048, 40-1024 and 160-2048 to 40-512 at each redshift, indicating the 20 per cent and 10 per cent scatter with light and dark grey bands, respectively.

readily to disparate data sets. Meyer et al. (2020) define a spike as a pixel at  $z \sim 6$  with a signal-to-noise ratio  $> 3$  (after convolution with a Gaussian, see their sec. 3 for details) and  $F > 0.02$ . With the spikes identified, Meyer et al. (2020) use the following estimator for the 2PCCF, originally due to Davis & Peebles (1983)

$$\xi(r) = \frac{n_R}{n_D} \frac{D_G D_S(r)}{R_G D_S(r)} - 1, \quad (\text{B1})$$

where  $D_G D_S$  is the number of galaxy-spike pairs as a function of  $r$ ,  $R_G D_S$  is the number of random-spike pairs (where the random positions are drawn from a uniform distribution) as a function of  $r$  and  $n_G$  and  $n_R$  are the total numbers of galaxy-spike and random-spike pairs, used for normalisation.

In Fig. B1 we show the galaxy-spike 2PCCF measured from our simulations, where we identify spikes as any pixel with  $F > 0.02$  and galaxies as haloes with  $M_h \geq 10^{10} h^{-1} M_\odot$ . We do not model observational effects (e.g., resolution or noise), deferring a study of their impact to future work. We now find excellent agreement between the 160-2048 model and the Meyer et al. (2020) correlation with LBGs (mostly  $< 1\sigma$ ) and slightly poorer agreement with their correlation with LAEs. As found in Sec. 3.2, for  $r \lesssim 20$  cMpc we find excellent agreement (always  $< 1\sigma$ ) between the 40-2048 and both the Meyer et al. (2020) LBG and LAE correlations, but poor agreement at larger  $r$ . The lack of a redshift mismatch also suggests that the most plausible explanation for the apparent tension with the

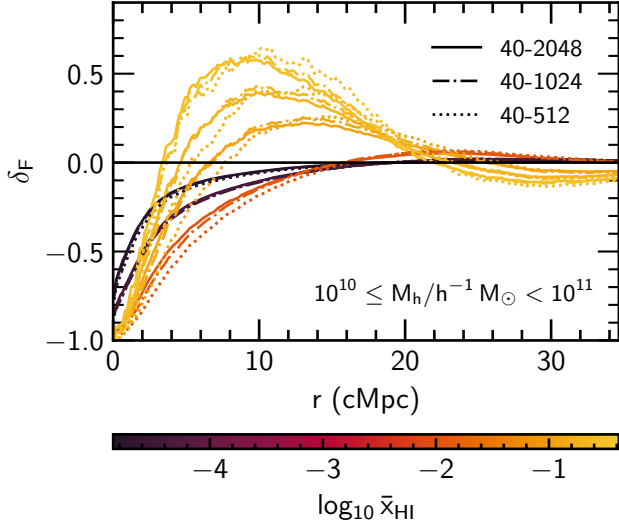


**Figure A2.** Galaxy–Ly  $\alpha$  transmission correlation as a function of distance  $r$  from haloes with mass  $10^{10} \leq M_h/h^{-1} M_\odot < 10^{11}$  for different Sherwood-Relics runs, compared at approximately equal volume-averaged neutral fraction  $\bar{x}_{\text{HI}}$ . We show the fiducial 40-2048 (solid) simulation with the 40-1024 (dot-dashed) and 40-512 (dotted) simulations, which have the same box size of  $40 h^{-1}$  Mpc but a particle mass that is 8 and 64 times larger, respectively, demonstrating the impact of mass resolution.

Meyer et al. (2019)  $\delta_F$  measurements is the uncertain CIV absorber bias, rather than differences in the reionisation history.

This paper has been typeset from a  $\text{\TeX}/\text{\LaTeX}$  file prepared by the author.

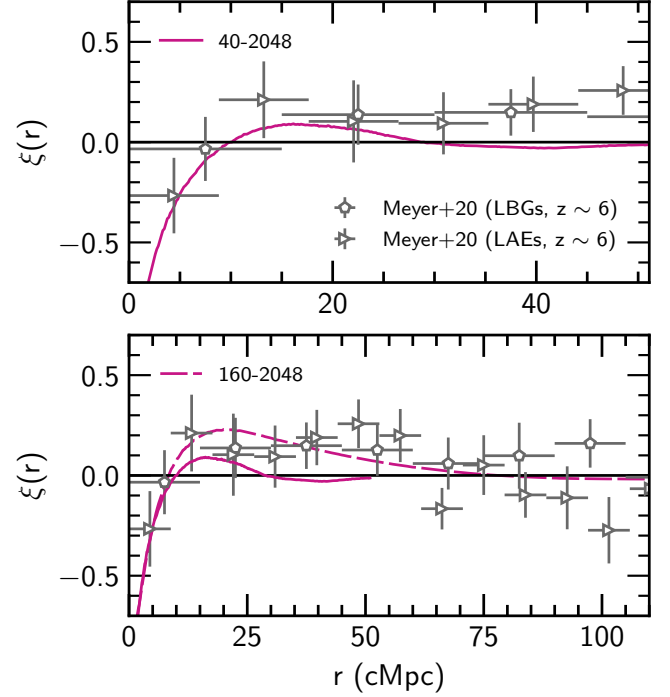


**Figure B1.** The two-point cross-correlation function between galaxies and transmission spikes at  $z = 6$  in the 40-2048 (solid, top and bottom panels) and 160-2048 (dashed, bottom panel) models. Also shown are the constraints due to Meyer et al. (2020) (grey points). Note the different ranges of  $r$  between the top and bottom panels.